Lawrence Berkeley National Laboratory

Title
The Isomer Ratio of Ce137m -Ce137g Produced in Several Charged-Particle Reactions

Permalink
https://escholarship.org/uc/item/1m0364b4

Author
Kiefer, Richard Leslie

Publication Date
1963-10-01

University of California

Ernest O. Lawrence Radiation Laboratory

THE ISOMER RATIO OF Ce^{137m}-Ce^{137g} PRODUCED IN SEVERAL CHARGED-PARTICLE REACTIONS

Berkeley, California

DISCLAIMER

UNIVERSITY OF CALIFORNIA

Lawrence Radiation Laboratory
Berkeley, California

Contract No. W-7405-eng-48

THE ISOMER RATIO OF Ce^{137m} - Ce^{137g} PRODUCED
IN SEVERAL CHARGED-PARTICLE REACTIONS

Richard Leslie Kiefer

(Ph.D. Thesis)

October 17, 1963

UNIVERSITY OF CALIFORNIA

Lawrence Radiation Laboratory
Berkeley, California

AEC Contract No. W-7405-eng-48

February 13, 1964

TO: All recipients of UCRL-11049 UC-4 Chemistry

FROM: Technical Information Division

Subject: UCRL-11049, "The Isomer Ratio of Ce^{137m} - Ce^{137g} Produced
in Several Charged-Particle Reactions," Richard Leslie Kiefer
(Ph. D. Thesis), October 17, 1963.

Please replace the following pages in your copies of UCRL-11049:

Pages - 47-48
Pages - 49-50
Pages - 51-52
Pages - 55-56
Pages - 57-58
Pages - 59-60
Pages - 61-62
Pages - 63-64
Pages - 69-70
Pages - 71-72
Pages - 73-74
Pages - 75-76
Pages - 77-78

Figure placement has been corrected.

THE ISOMER RATIO OF Ce^{137m} - Ce^{137g} PRODUCED IN SEVERAL CHARGED-PARTICLE REACTIONS

Contents

THE ISOMER RATIO OF Ce^{137m} - Ce^{137g} PRODUCED IN SEVERAL CHARGED-PARTICLE REACTIONS

Richard Leslie Kiefer

Lawrence Radiation Laboratory
University of California
Berkeley, California

October 17, 1963

ABSTRACT

The isomer ratio of Ce^{137m} - Ce^{137g} is studied to obtain information on the effect of angular momentum in the de-excitation of a compound nucleus. The ratio of the formation cross section of the high-spin isomer to that of the low-spin isomer is measured as a function of energy for reactions induced by He^3, He^4, Li^7, and C^{12}. The ratio is seen to increase with increasing projectile energy. This increase is shown to correspond to an increase in the average angular momentum. The ratio at the peak of the excitation function is found to increase linearly from reaction to reaction with increasing $\langle \ell \rangle$. Above the peak of the excitation function, the ratio is observed to increase more rapidly. This is considered to be due to the competition of neutron and γ - ray emission that causes the product to be formed from states of high angular momentum.

The cross sections are also measured for the four reactions. Those induced by Li^7 and C^{12} peak 5 to 6 MeV above the cross sections induced by He^3 and He^4.

The results are compared with calculations based on the Huizenga-Vandenbosch theory. When we calculated the nuclear temperature based on the Fermi gas model and used 0.7 of the rigid-body value of the moment of inertia, the calculated results showed good agreement with the experimental results. Calculations employing a simple pairing model and a superconductor model are also shown.

I. INTRODUCTION

Nuclear isomers were discovered in 1921 by Hahn when he showed that UZ (Pa^{234}) and UX$_2$ both grew out of UX$_1$ (Th^{234}) by beta decay.[1] This remained as a curiosity until 1935 when the first artificially produced isomeric pair Br^{80m} and Br^{80g}, was verified.[2] The following year, von Weizsäcker gave a theoretical explanation of isomerism.[3] He proposed that a nuclear isomer was a metastable excited state in a nucleus. By assigning a spin difference of up to five between the excited and ground states, and allowing an energy difference of a few kilovolts he showed that the half-life for γ-ray de-excitation of the upper state was comparable to that of observable isomers.

For odd-A nuclei, there are three regions or "islands" of isomerism.[4] The first occurs where the number of neutrons or protons, whichever is odd, is between 39 and 49. In this region, the shell model predicts that the $p_{1/2}$ and $g_{9/2}$ states will lie close to each other in energy and will compete for the position of ground state. Thus, the ground state and first excited state will have a spin difference of 4. Similarly, the next region exists where the odd-nucleon number is between 65 and 81. Here, the $h_{11/2}$ state lies close to the $d_{3/2}$ and $s_{1/2}$ states. The third region appears where odd-number nuclei have neutron numbers ranging from 101 to 126. The $i_{13/2}$ and $f_{5/2}$ states cause isomerism in this area. Approximately 120 cases of isomerism are known in these three regions.

There have been numerous studies of nuclear reactions in which an isomeric pair is produced. In nearly all of these, the main interest is in comparing the formation cross section of the isomer with that of the ground state. The ratio σ_m/σ_g is commonly called the isomer ratio. Wing has tabulated the data in this field up to 1962.[5] Some studies have used low-energy neutrons to produce the reaction.[6,7] Segrè and Helmholz, in a review article, suggested that as the energy of captured neutrons is increased so that capture occurs over many levels each of which has a different angular momentum, the influence of the level in which capture occurs will diminish, and in the limiting case only the statistical weights (2 I + 1) of the isomeric states will determine their formation

cross sections.[6] Thus, the ratio of the formation cross section of the isomer to that of the ground state should approach $(2 I_m + 1)/(2 I_g + 1)$, where I_m and I_g are the spins of the metastable and ground states respectively. In extending this argument to charged-particle reactions, Levy proposed that no such limit should exist.[8] He reasoned that the total angular momentum of a compound system is the vector sum of the spin of the target nucleus, the spin of the projectile, and the angular momentum (ℓ) that is carried into the reaction by the projectile. As the energy of the projectile is increased, thus increasing ℓ, the distribution of nuclear states available for capture will become broader. The states of higher spin will be favored because of their statistical weights $(2 I + 1)$. Since emitted particles cannot take away large amounts of angular momentum, and the γ - ray cascade is composed of dipole and quadrupole radiation, the amount of high-spin isomer should be increased with increasing projectile energy. By this argument, there would be no limiting value of the isomer ratio. Levy showed that with 23-MeV α particles incident on manganese to produce the cobalt-58 isomers, the ratio $\frac{\sigma_m}{\sigma_g}$ went beyond the limit predicted by Segrè. Meadows, Diamond, and Sharp reported the isomer ratios of Br^{80}, Co^{58}, and Sc^{44} produced in (p,pn) reactions.[9] The incident-proton energies ranged from threshold to 100 MeV. In the low-energy region they found that the cross-section ratio of the metastable state to the ground state increased beyond the ratio of statistical weights. As the energy was increased, however, the value went below the statistical "limit" and remained constant as high as 100 MeV. They assumed that at low energies a compound-nucleus mechanism prevailed. At higher energies, they interpreted their results to mean that the reaction proceeded by a knock-on mechanism such as the one proposed by Serber.[10]

Calculations to predict the isomer ratio have been shown by various authors.[9,11,12,13] Katz, Pease, and Moody computed the distribution of orbital angular momentum, ℓ, by using the relationship[11]

$$\sigma_\ell (E) = \frac{1}{2} (2 \ell + 1) \, \tilde{\lambda}^2 \, T_\ell (E) , \tag{1}$$

where $T_\ell(E)$ = transmission coefficient for a given ℓ at an incident
energy E ,

$\lambdabar$ = the de Broglie wavelength of the incoming projectile
divided by 2π ,

and $\sigma_\ell(E)$ = cross section for compound-nucleus formation with a given
ℓ at energy E.

Thus, an average ℓ was obtained and combined with the projectile and
target spins to give a total angular momentum J. Then they assumed
that every compound nucleus formed with a total angular momentum below
a certain cutoff value goes to the low-spin isomer, whereas the remainder
feeds the high-spin partner. They determined the cutoff value by the
spins of the two isomers, and obtained results that are in fair agreement
with experiments for a number of low-energy reactions producing Br^{80}.
Sylvia Bailey, using a similar approach, calculated the isomer ratio of
Sc^{44}.[12] From Eq. (1) she computed a spin distribution after each particle
emission from the compound nucleus. This same expression was used to cal-
culate the initial spin distribution caused by the incoming projectile.
The nuclear level density, which is important when considering particle
or γ-ray emission, was assumed to be proportional to $2J + 1$. Meadows,
Diamond, and Sharp also performed calculations relating the isomer ratio
to the initial angular-momentum distribution and the spins of the two
isomers.[9] They used an exponential level-density relationship based on
the Fermi gas model. Huizenga and Vandenbosch proposed a more detailed
calculation relating the isomer ratio more quantitatively to the spin
dependence of the nuclear level density and the multiplicity and multipole
character of the γ-ray cascade.[13] Details of this calculation are shown
later with a tabulation of results calculated by this method. The com-
parison of these results with experimental values is shown.

We have seen that the isomer ratio can be related to processes
involved in the mechanism of compound-nucleus formation and de-excitation.
These processes are known to be affected by angular momentum.[14,15,16]
Large amounts of angular momentum are brought into a compound-nucleus system
when a heavy ion $(z > 2)$ is used as the bombarding projectile. The

Berkeley heavy-ion linear accelerator (Hilac) is a convenient source of various heavy-ion beams. This work was undertaken to learn more about the effect of angular momentum in a compound-nucleus reaction. We decided to produce a pair of isomers with both heavy-ion and light-particle reactions. If the initial compound nucleus in each reaction were at the same excitation energy, any difference in the isomer ratio should be due to angular momentum.

The isomeric pair we have chosen to study is Ce^{137m}; Ce^{137g}. Several reasons governed this choice: (a) the half-lives are long enough (35 h and 9 h) to permit chemical separation before counting; (b) the decay scheme has been well studied;[17] and (c) enough stable target isotopes are available that the compound nucleus can be produced with various bombarding particles. We studied four reactions with Ce^{140} as the compound nucleus. The variation of the isomer ratio with excitation energy is presented for each case.
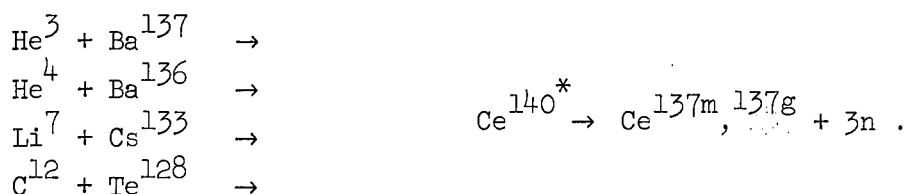
Other workers have also studied this isomeric pair. Vignau and Nassiff looked at the reaction $La^{139}(d,4n)Ce^{137}$.[18] They plot the isomer ratio as a function of energy over a deuteron energy range of 18 MeV to 27 MeV. Keisch has observed the ratio, Ce^{137m}/Ce^{137g}, produced by neutron activation of Ce^{136}.[7] Choppin and Klingen have shown that the excitation function for the $C^{12}(Te^{128}, 3n)Ce^{137m}$ reaction peaks at 13 MeV higher than predicted by a theory that assumes no angular momentum.[16] Mollenauer finds that when high-energy (100 MeV) C^{12} ions are incident on natural tellurium, the total γ-ray energy is higher than the binding energy of the next neutron.[14] Morton, Choppin, and Harvey arrive at a similar conclusion based upon studies of angular distribution and range of the $C^{12}(Te^{130},5n)Ce^{137m}$ reaction.[19]

In summary, the purpose of this work is to obtain information on the effect of angular momentum in a nuclear reaction by producing a pair of nuclear isomers with varying amounts of angular momentum, then to compare the experimental work with a statistical theory to relate the spin dependence of the nuclear level density to the ratio of nuclear isomers.

II. EXPERIMENTAL PROCEDURES

A. Target Preparation and Irradiation

The isomer ratio of Ce^{137m} - Ce^{137g} was measured in four different reactions:

$$He^3 + Ba^{137} \rightarrow$$
$$He^4 + Ba^{136} \rightarrow$$
$$Li^7 + Cs^{133} \rightarrow \qquad Ce^{140*} \rightarrow Ce^{137m, 137g} + 3n \ .$$
$$C^{12} + Te^{128} \rightarrow$$

The target foils were prepared from enriched isotopes in various ways. The Ba^{137} targets, enriched to 81.9%, were made by repeatedly brushing a solution of $Ba^{137}(NO_3)_2$ onto 0.5-mil Cu foil, with heating between each application. Thicker Ba^{136} targets, enriched to 92.9%, were made by successive application of a $Ba^{136}(NO_3)_2$ solution to Cu foils 1.0 mil thick with a micropipet. Cesium-133 targets were made by evaporating $CsNO_3$ onto Cu foils 0.2 mil thick under vacuum. These targets contained 100% Cs^{133}, the only stable isotope of cesium. Tellurium-128, enriched to 96.4% was electroplated onto thin (0.05 mil) Cu foils from a dilute nitric acid solution. Details of the target preparations are described in Appendix A.

The stacked-foil method with eight foils was used in all the irradiations. The individual foils were separated with aluminum rings that prevented the foils from sticking together but did not interfere with the beam. Aluminum foils, whose thickness was determined by weighing a known area, were used to lower the incident-beam energy to the desired amount at the first target foil. The range-energy data used are plotted in Appendix B.

The He^4 irradiations were performed at the 60-inch cyclotron. The maximum-energy He^4 ions have a range of 231 ± 5 mg/cm^2 in aluminum,[20] which correspond to an energy of 47.6 ± 0.5 MeV.[21] The water-cooled copper target holder was electrically insulated from the machine, and grounded so that the accumulation of charge could be measured by an electrometer. The

beam intensity was limited to 0.2 μA to prevent holes from being burned into
the foils.

The other irradiations were carried out at the Hilac, where ions
are accelerated to a terminal energy of 10.4±0.2 MeV/nucleon.[22] An
electrometer measured the charged collected by the insulated copper target
holder. Collimators on the target holder and the end of the accelerator
defined the beam that passed through the foils. Beam intensity varied
with the ion. The C^{12} beam was limited to 1 μA to prevent the foils from
being burned. No beam limit was necessary in the He^3 and Li^7 irradiations
in which the average He^3 beam current was 0.7 μA, whereas that of Li^7
was 0.09 μA. The Li^7 beams were of much lower intensity because of the
difficulty of maintaining a constant supply of lithium ions.

B. Chemistry and Sample Preparation

After the targets were irradiated, the radioactive cerium was
chemically separated from the remaining target material. The procedure
used was a modified form of the one used by Glendenin.[23] It utilizes the
circumstance that cerium is more easily oxidized from the +3 to the +4
state than any other lanthanide. In the +4 state, it can be extracted
from a strong nitric acid solution with methyl isobutyl ketone (hexone).
Thus, the targets (including backing foil) were dissolved in concentrated
HNO_3. The cerium was oxidized with sodium bromate, extracted into hexone,
reduced with H_2O_2 , and precipitated as cerium oxalate nonahydrate
$Ce_2(C_2O_4)_3 \cdot 9 H_2O$. The precipitate was collected on a glass-fiber filter
disk, dried, weighed, and mounted on an aluminum counting plate. Details
of the chemistry and sample preparation are given in the appendices.

It has been shown that HCl greatly accelerates the reduction of
Ce^{+4}.[24] Since it is necessary to have cerium in the +4 state in the early
part of the chemical separation, the use of HCl is to be avoided. For this
reason, copper foil was used as the backing material for the targets be-
cause it can be readily dissolved without HCl.

C. Counting Procedure

The relative and absolute amounts of the Ce^{137} isomers were established by counting the γ rays characteristic of their decay. The decay scheme is shown in Fig. 1.[17]

The counter was a thallium-activated sodium iodide crystal 3 in. high and 3 in. in diameter, which was attached to a duMont #6363 photo-multiplier tube. The entire unit, including a polystyrene β-ray absorber, was purchased as an "Integral Line" assembly from the Harshaw Company. The rest of the counting apparatus consisted of a preamplifier, which was attached to the photomultiplier tube, a linear amplifier, and a 100-channel pulse-height analyzer. The resolution of the counter with the 662-keV γ ray of Cs^{137} was 8.1%.

The crystal assembly was housed in a lead cave lined both with 30-mil cadmium foil to absorb the lead K x rays, and 15-mil copper foil to absorb the cadmium x rays.[25]

A Plexiglass sample holder supported the crystal assembly in the cave. Slots cut in the sides positioned the samples at various distances from the crystal face. The samples counted in this work were placed in the upper most slot, which put them about 0.6 cm from the crystal. At this distance, 38.8% of the disintegrations are incident on the crystal face. Thus, the geometry factor for this shelf is 0.388. A curve of geometry factor vs shelf number for this counting assembly appears in Appendix D.

Before the samples were counted, various sources of known energy were counted and the channel number corresponding to the peak of each was noted. From this, a curve of channel number vs energy was drawn so the energies could be assigned to the peaks in the spectra. This also tests the linearity of the amplifier response.

The γ-ray spectrum of the samples changed with the energy of bombardment. At the lower energies a prominent peak appeared at 255 keV, which was characteristic of the isomeric transition, and another at 445 keV, which was characteristic of the ground-state decay. On the
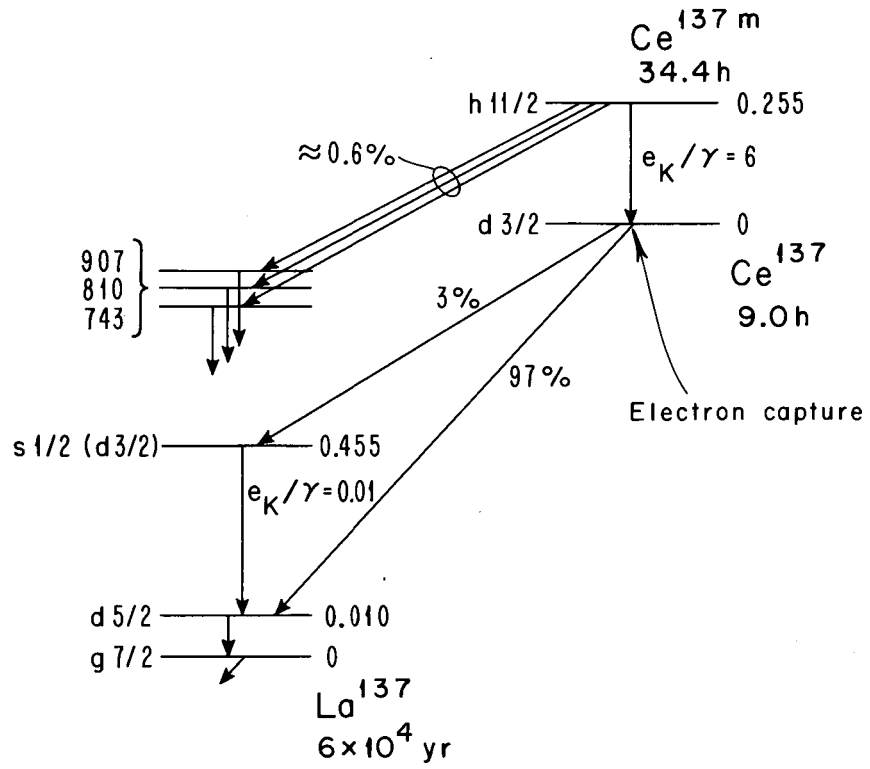
Fig. 1. The decay scheme of Ce^{137} taken from Ref. 17.

higher peak appeared a shoulder due to the 511 keV annihilation radiation of Ce^{135}. As the energy was increased, the average angular momentum was also increased, and the formation of the high-spin metastable state was increased at the expense of the low-spin ground state. At the same time, the yield of the five-neutron reaction producing Ce^{135} was increasing. The limit in the experiments occurred when the 511-keV annihilation radiation peak of Ce^{135} enveloped the diminishing 445-keV peak of Ce^{137}. The limit occurred at an excitation energy of 50 MeV. Since maximum-energy He^{3} and He^{4} ions produced excitation energies less than 50 MeV, this problem was encountered only in the C^{12} and Li^{7} irradiations. The reaction Q values used for the excitation energies were calculated from the mass tables of Seeger.[26]

An example of the spectrum produced at an excitation energy of 40 MeV is shown in Fig. 2. The highest-energy peaks were assumed to be those which Danby lists at 743, 810, and 901 keV (see Fig. 1).[7] This group decayed with the 34.4-h half-life of the Ce^{137} metastable state.

Figure 3 shows the spectrum produced in reactions at an excitation energy of 50 MeV. The 445-keV peak is almost entirely absorbed in the background. The lowest-energy peak contains contributions from the 225-keV γ ray of Ce^{137} and the 265-keV γ ray that is prominent in the spectrum of Ce^{135}.[27] The peaks at 300, 511, and 600 keV all decayed with the 22-h half-life of Ce^{135}. This spectrum appears to contain high-energy peaks similar to those found in Fig. 2. However, in this case the peaks decay with the Ce^{135} half-life. Apparently, the two Ce isotopes have similar high-energy γ rays.

In order to check the decay of the peaks, the samples were counted for at least 6 days. This allowed the 34.4-h state to decay through four half-lives.

D. Data Processing

The activity of the isomers was determined by using the decay of the 445-keV peak. Each count of a sample was plotted on semilog graph paper and the area under the peak determined by graphical integration. It was assumed that the photopeak in a γ-ray spectrum was Gaussian.[25] For consistency, a Gaussian template was used to determine the boundaries of
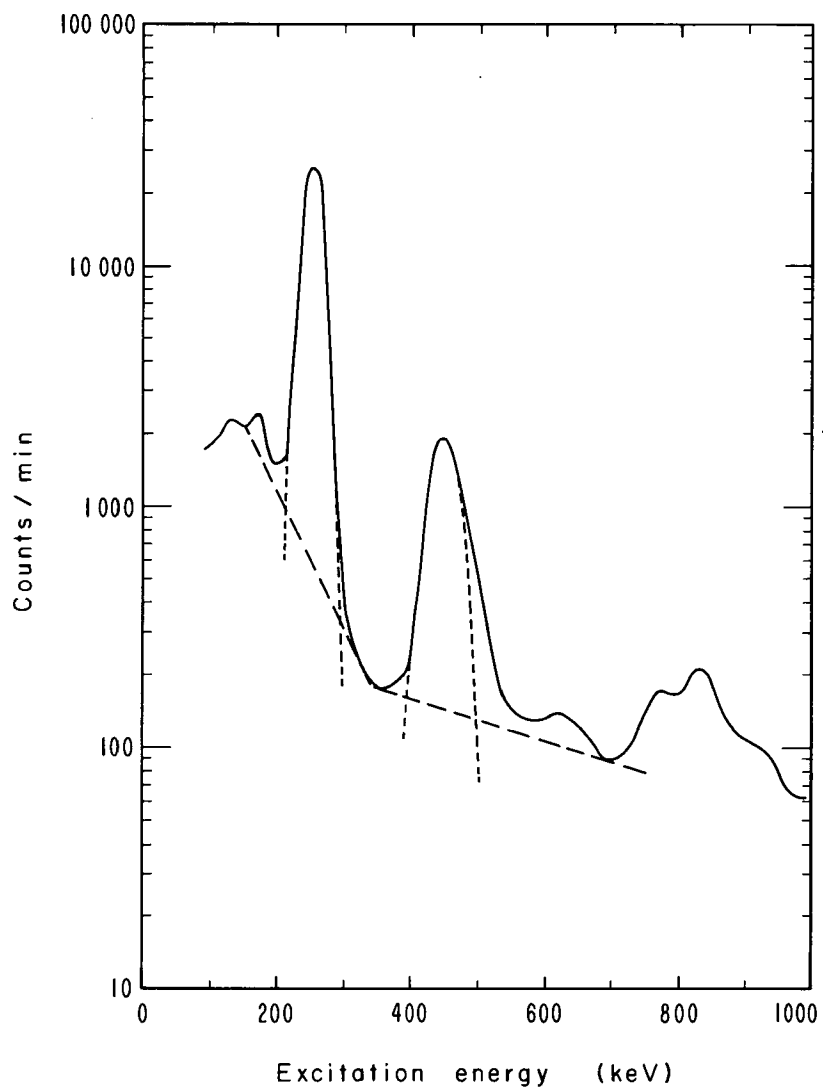
MU-32208

Fig. 2. Typical gamma-ray spectrum of a sample produced with an
   excitation energy of 40 MeV.
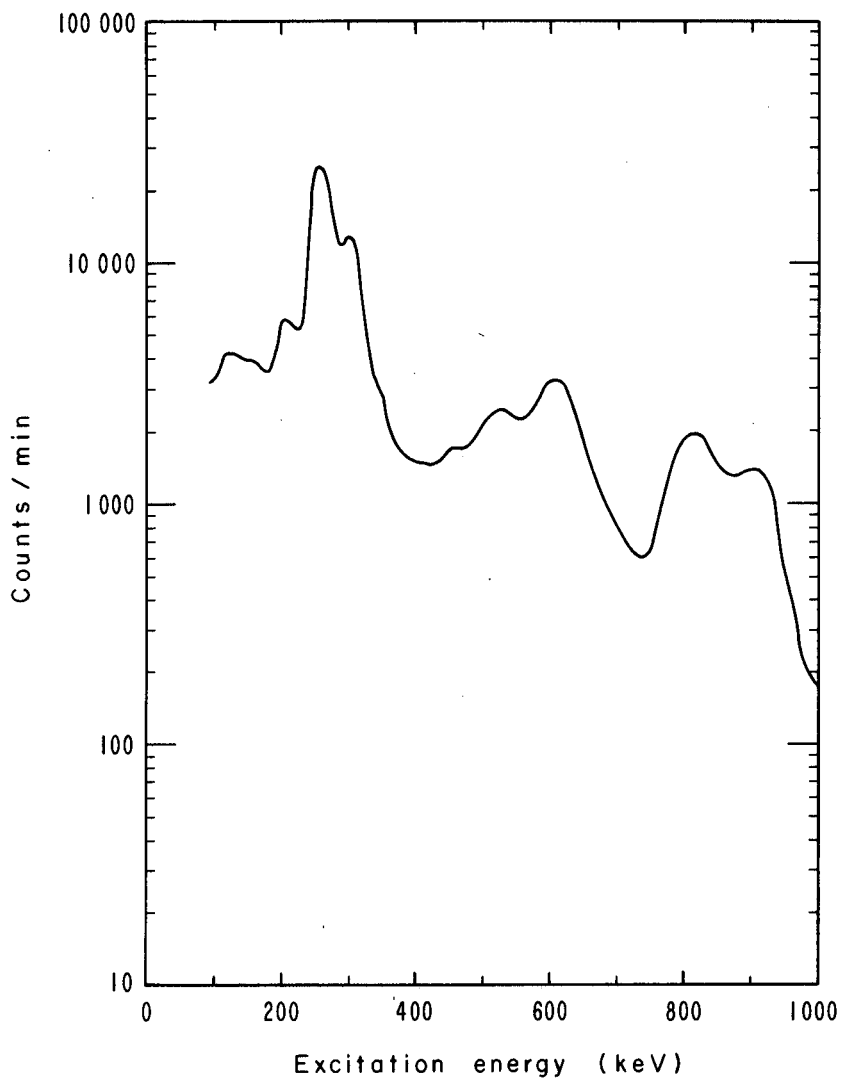
Fig. 3. Typical gamma-ray spectrum of a sample produced with an
excitation energy of 50 MeV.

the 445-keV peak in all the samples. A background line was drawn along
the base of the peak to separate it from the Compton edges of higher-
energy γ rays (see Fig. 2). Initially, the line was determined by count-
ing a series of monoenergetic γ-ray standards and plotting the results on
individual semilog graphs. The plotted standard, whose energy was closest
to that of the highest-energy peak of the spectrum, was positioned beneath
the spectrum graph to coincide with the peak height. It was then sub-
tracted point by point to simulate the subtraction of the Compton edge of
the peak. The process was repeated for each peak in the spectrum until
the 445-keV peak was reached. The background line was determined by
points representing values of the subtracted Compton edges plus the
natural background. These were subtracted from every point under the
445-keV peak along with any contribution from the 511-keV photopeak.

After the activity was determined for each count, the data were
plotted as a function of time from the end of bombardment. When the
bombarding energy was high, the high spin state was formed in preference
to the low-spin state so that the resulting curve grew to a maximum and
diminished with a 34.4-h half-life, as illustrated in Fig. 4. At low
bombarding energies, where the formation of the ground state is about
equal to that of the metastable state, the curve begins high and levels
off to a 34.4-h half-life as shown in Fig. 5.

A composite decay such as this is treated by the equation[28]

$$N_2 = [\lambda_1/(\lambda_2 - \lambda_1)] N_1^0 [\exp(-\lambda_1 t) - \exp(-\lambda_2 t)] + N_2^0 \exp(-\lambda_2 t),$$

(2)

where N_2 is the number of ground-state nuclei present at time t from
the end of bombardment, N_1^0 and N_2^0 are the number of isomer and ground-
state nuclei present at the end of bombardment, and λ_1 and λ_2 are
the decay constants. When activities are substituted for numbers of
nuclei, Eq. (2) becomes
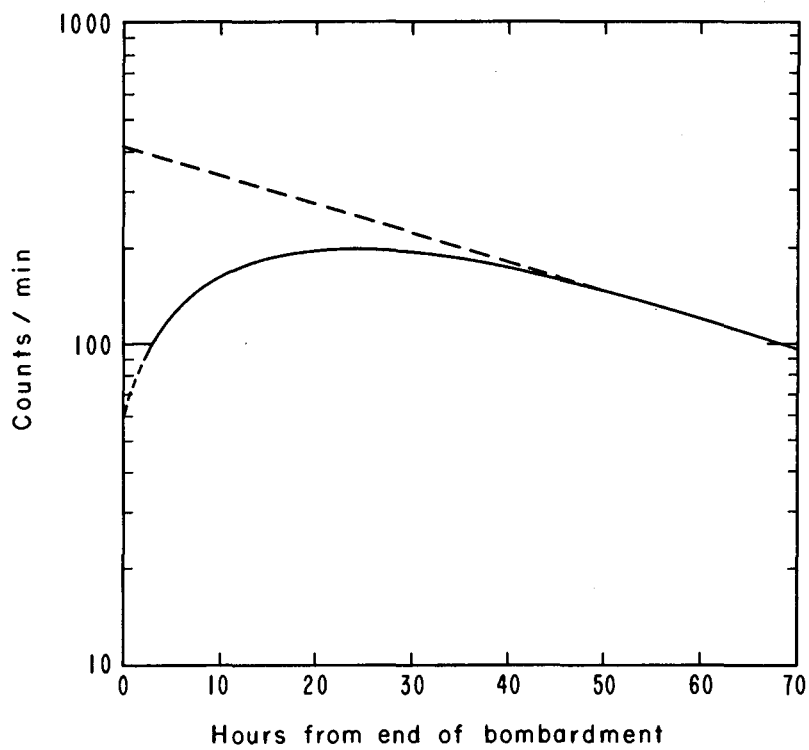
Fig. 4. Decay of the 445 keV peak in a sample produced at high-
excitation energy. The solid line is drawn through the data
points and the dashed line is the extrapolation to zero time.

Fig. 5. Decay of the 445 keV peak in a sample produced at low-excitation energy. The solid line is drawn through the data points and the dashed line is the extrapolation to zero time.
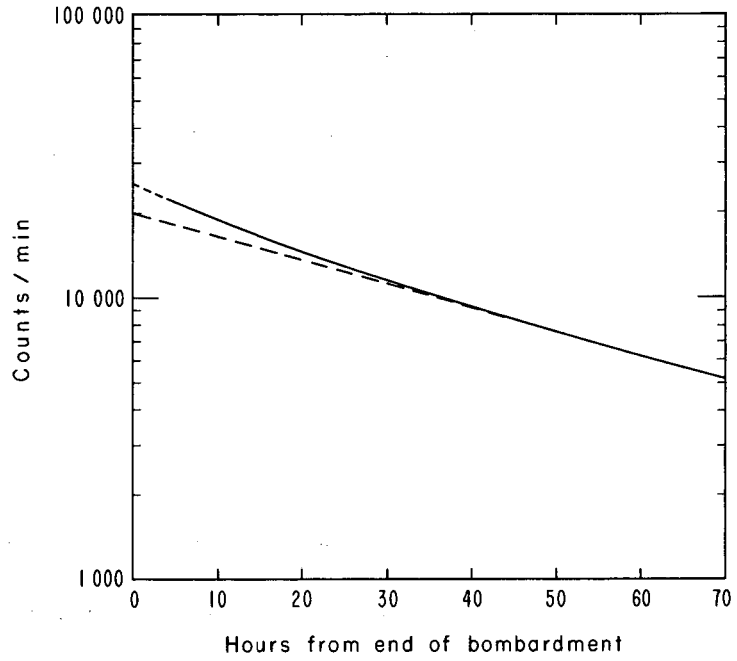
$$A_2 = [\lambda_2/(\lambda_2 - \lambda_1)] \, A_1^{\,0}[\exp(-\lambda_1 t) - \exp(-\lambda_2 t)] + A_2^{\,0} \exp(-\lambda_2 t) \, .$$

$$(3)$$

where the notation is similar. When t = 0, Eq. (3) reduces to $A_2 = A_2^{\,0}$. Thus, the initial activity of the ground state is determined by extrapolating the curves in Figs. 4 and 5 to zero time. At sufficiently large t, the $\exp(-\lambda_2 t)$ term is negligible compared with the $\exp(-\lambda_1 t)$ part, so that

$$A = [\lambda_2/(\lambda_2 - \lambda_1)] \, A_1^{\,0} \exp(-\lambda_1 t).$$

$$(4)$$

Extrapolating this to t = 0 gives

$$A_2 = [\lambda_2/(\lambda_2 - \lambda_1)] \, A_1^{\,0} \, ,$$

$$(5)$$

and the initial activity of the metastable state is determined. This extrapolation is shown as a dashed line in Fig. 4.

Since the initial activities of the two isomers were determined from the same γ - ray peak, the various counter corrections were unnecessary in the ratio. Thus, the ratio of cross sections becomes $(A_m/\lambda_m)/(A_g/\lambda_g)$ times a correction for decay during bombardment. This correction is shown in Appendix D.

The activity due to the isomer was also determined by graphical integration of the 255-keV peak. To determine the isomer ratio with two different peaks, corrections must be made for the differences in counter efficiency and peak-to-total ratio and for any branching ratios and conversion coefficients connected with the peaks. After making these corrections, the isomer ratio measured from the 255-keV and 445-keV peaks was compared to that measured from the 445-keV peak alone. The former ratios were about 20% higher than the latter ones over the entire range of energies and reactions. It was assumed that either the published conversion coefficient of the 255-keV peak or the branching ratio to the 445-keV peak was in error. To eliminate any decay scheme inaccuracies, the ratios were determined by using only the 445-keV peak.

Figures 4 and 5 show the necessity of counting the samples soon after the end of bombardment in order to make an accurate extrapolation to zero time. Since it took at least 2 hours to transport the target from the cyclotron, perform the chemistry, and mount the samples, the extrapolations were made by using a least-squares computer program. The half-life of the isomer was checked by using the FRENIC program to analyze the decay of the 255-keV peak. Guesses of the decay constant and ordinate intercept are included in the input along with the data, and the best intercept and decay constant are calculated. The half-life obtained from the decay constant was averaged for all the experiments and found to be 34.0 ± 1.1 h, which is in good agreement with the published value of 34.4 ± 0.3 h.[17] Another program, LENIC, was used to analyze the 445-keV data. Guesses about the intercepts are not necessary with this program, but the decay constants cannot be varied. The average λ from FRENIC was used for the metastable state, and a λ corresponding to a half-life of 9.0 h was used for the ground state. Appendix E contains some details of the programs.

Both computer programs treated the data points as having equal statistics. In general, the samples were counted to approximate this situation. However, in the high-energy samples of the C^{12} and Li^{7} irradiations there were large contributions from Ce^{135}. As this part decayed away, the counting statistics for Ce^{137} did not remain constant. Since the Ce^{137} counting rates were low, the differences became important in the computer analysis. Thus, these data were analyzed by a graphical method.[29] Both sides of Eq. (3) were divided by $\exp(-\lambda_2 t)$ to give

$$A_2 \exp(\lambda_2 t) = [\lambda_2/(\lambda_2 - \lambda_1)] A_1^{0} \{\exp[(\lambda_2 - \lambda_1)t] - 1\} + A_2^{0} .$$

(6)

A plot of $A_2 \exp(\lambda_2 t)$ vs $\exp[(\lambda_2 - \lambda_1)t] - 1$ is a straight line of slope $A_1^{0} \lambda_2/(\lambda_2 - \lambda_1)$ and ordinate intercept A_2^{0}. For consistency, all of the Li^{7} and C^{12} data were analyzed in this manner. A comparison of the two methods with the lower-energy samples showed them to be compatible.

An initial attempt to determine the isomer ratio by counting the x-rays from electron conversion and electron-capture events was unsuccessful, as most of the neutron-deficient cerium isotopes decay partially by electron capture. Also, the conversion coefficient of many cerium γ rays is not known.

III. RESULTS AND DISCUSSION

A. Isomer-Ratio Results

The experimentally determined Ce^{137m} - Ce^{137g} isomer ratios are tabulated in Tables I through IV. With one exception, the values are all greater than 1, indicating that in the energy region studied, the high-spin metastable state is more likely to form than the low-spin ground state. For comparison, it is interesting to note that the statistical "limit" $(2I_m + 1)/(2I_g + 1)$ is 3 for this system. The variation of the isomer ratio with excitation energy for the four reactions studied is shown in Figs. 6 through 9.

B. Cross Sections

In some of the experiments performed, cross-section measurements were also made. The results for the metastable and ground states are shown in Figs. 10 through 13. A comparison of the combined metastable and ground-state cross sections is shown in Fig. 14. The cross sections of the Li^7- and C^{12}- induced reactions peak appreciably higher than those induced by the lighter projectiles. Also, as Figs. 12 and 13 show, the peak of the metastable-state cross section is about 2 MeV above that of the ground state for these two reactions.

The cross sections of the He^3- and C^{12}- induced reactions fall off rapidly on the low-energy side of the peak. This is probably an effect of the Coulomb barrier. Table V lists the Coulomb barrier and reaction threshold in laboratory-system energy and the corresponding excitation energy for the reactions studied.

C. Errors

The errors quoted in the He^4 and He^3 isomer-ratio results are derived mainly from the standard deviations calculated by the least-squares computer analysis of the data. The number of atoms formed in both

Table I. Experimental results for the reaction
$He^4 + Ba^{136} \rightarrow Ce^{137} + 3n$.

Experiment	Projectile energy (laboratory system) (MeV)	Excitation energy (MeV)	Isomer ratio Ce^{137m}/Ce^{137g}
A	45.8	45.9	12.0 ± 1.1
	43.7	43.9	11.1 ± 1.0
	41.6	41.8	9.7 ± 1.2
B	46.7	46.8	12.0 ± 2.1
	44.4	44.5	11.7 ± 1.6
	42.0	42.2	10.2 ± 1.3
	39.5	39.7	6.2 ± 1.5
	36.3	36.7	4.5 ± 1.0
	33.7	34.2	4.0 ± 0.7
	30.6	31.2	2.0 ± 0.3
	27.9	28.6	1.9 ± 0.1
C	37.7	38.1	7.0 ± 0.9
	28.4	29.1	2.0 ± 0.1
D	47.7	47.7	15.6 ± 2.4
	45.5	45.6	12.9 ± 1.4
	43.1	43.3	9.6 ± 0.9
	40.5	40.8	8.0 ± 0.6
	37.6	38.0	6.0 ± 0.3
	34.5	35.0	4.5 ± 0.2
	31.3	31.9	2.9 ± 0.1
	28.0	28.7	2.1 ± 0.2

Table II. Experimental results for the reaction
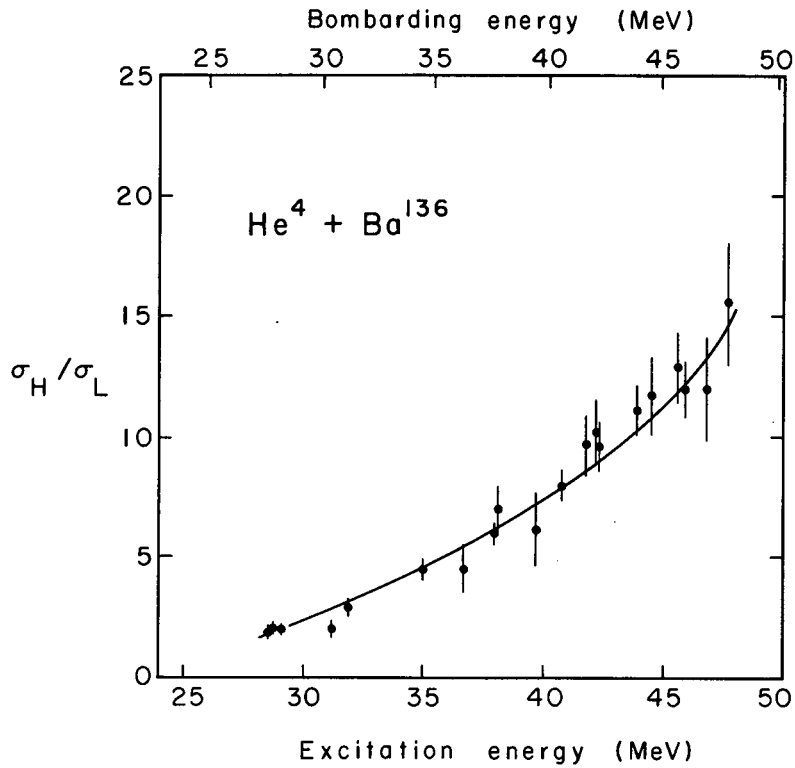$He^3 + Ba^{137} \rightarrow Ce^{137} + 3n$.

Experiment	Projectile energy (laboratory system) (MeV)	Excitation energy (MeV)	Isomer Ratio Ce^{137m}/Ce^{137g}
E	31.0	46.0	3.8 ± 0.2
	29.6	44.6	3.5 ± 0.2
	28.5	43.5	3.4 ± 0.2
	27.7	41.8	2.8 ± 0.1
	25.1	40.2	2.4 ± 0.1
	23.7	38.8	2.3 ± 0.2
	21.8	37.0	1.7 ± 0.1
	20.5	35.7	1.5 ± 0.1
F	29.3	44.3	3.3 ± 0.1
	27.8	42.8	3.0 ± 0.1
	26.4	41.4	2.6 ± 0.1
	24.8	39.9	2.2 ± 0.2
	23.1	38.3	1.9 ± 0.1
	21.4	36.6	1.5 ± 0.1
	19.6	34.8	1.3 ± 0.1
	17.6	32.8	1.1 ± 0.1
G	28.3	43.3	2.7 ± 0.4
	27.0	42.0	2.4 ± 0.3
	25.9	41.0	2.1 ± 0.3
	24.3	39.4	2.0 ± 0.2
	22.7	37.9	1.6 ± 0.2
	21.3	36.5	1.4 ± 0.1
	19.6	34.8	1.1 ± 0.1
	17.8	33.0	0.9 ± 0.1

Table III. Experimental results for the reaction
$$C^{12} + Te^{128} \rightarrow Ce^{137} + 3n.$$

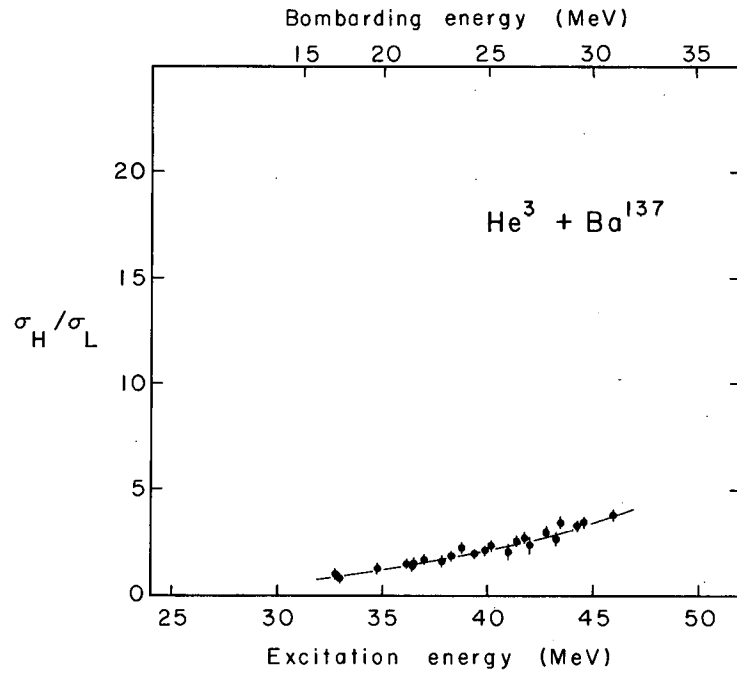| Experiment	Projectile energy (laboratory system) (MeV)	Excitation energy (MeV)	Isomer ratio Ce^{137m}/Ce^{137g}
H	54.9	50.0	20.7 ± 3.9
	50.3	45.8	5.2 ± 0.3
J	54.3	49.5	17.5 ± 1.3
	51.7	47.1	8.0 ± 0.8
	49.7	45.3	5.7 ± 0.3
	47.5	43.3	3.7 ± 0.2
	44.5	40.6	1.5 ± 0.3
K	54.7	49.9	20.2 ± 2.9
	52.2	47.6	7.6 ± 0.6
	50.4	46.0	6.6 ± 0.4
	45.7	41.7	2.0 ± 0.2

Table IV. Experimental results for the reaction
$Li^7 + Cs^{133} \rightarrow Ce^{137} + 3n$.

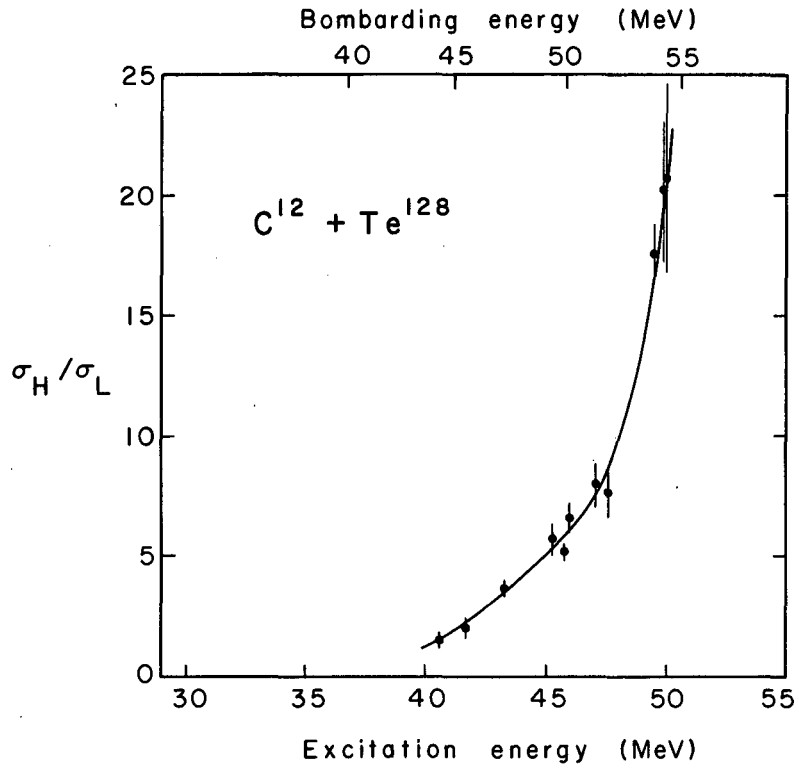| Experiment	Projectile energy (laboratory system) (MeV)	Excitation energy (MeV)	Isomer ratio Ce^{137m}/Ce^{137g}
L	37.3	50.2	12.4 ± 1.9
	34.9	47.9	7.3 ± 0.6
	32.3	45.5	5.9 ± 0.4
	30.3	43.6	4.6 ± 0.2
M	37.5	50.4	12.5 ± 1.6
	31.1	44.3	5.1 ± 0.4
	28.8	42.2	3.6 ± 0.3
	25.8	39.3	2.5 ± 0.2
	22.7	36.4	1.7 ± 0.1
N	35.1	48.1	7.3 ± 0.6
	33.4	46.5	5.8 ± 0.4
	31.6	44.8	5.1 ± 0.3
	29.9	43.2	3.9 ± 0.3
	27.9	41.3	3.2 ± 0.2
	25.7	39.2	2.4 ± 0.2
	22.8	36.4	2.0 ± 0.2

Fig. 6. The experimentally determined isomer ratios for the reaction $He^4 + Ba^{136} \rightarrow Ce^{137,137m} + 3n$, as a function of the excitation energy. The upper scale shows the laboratory energy of the projectile. The solid line connects the points.
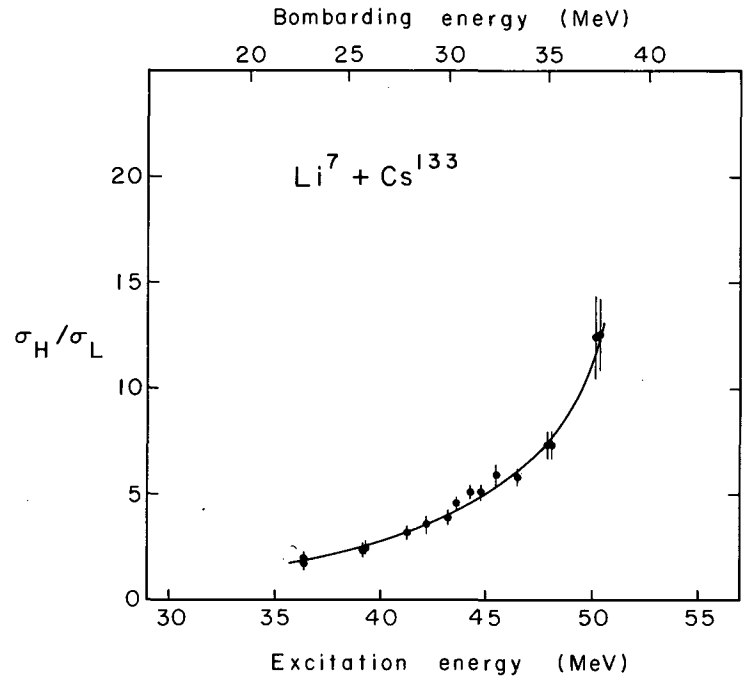
Fig. 7. The experimentally determined isomer ratios for the reaction
He^3 + Ba^{137} → Ce^{137,137m} + 3n, as a function of the excitation
energy. The upper scale shows the laboratory energy of the pro-
jectile. The solid line connects the points.

Fig. 8. The experimentally determined isomer ratios for the reaction $C^{12} + Te^{128} \rightarrow Ce^{137,137m} + 3n$, as a function of the excitation energy. The upper scale shows the laboratory energy of the projectile. The solid line connects the points.
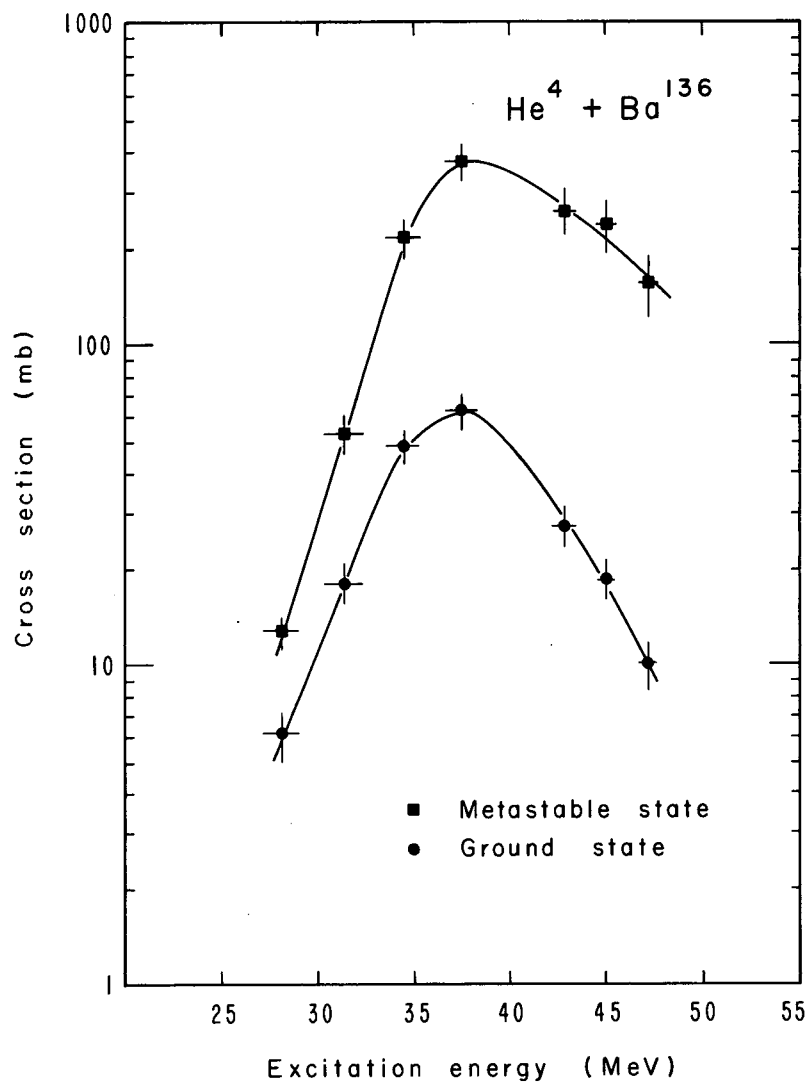
Fig. 9. The experimentally determined isomer ratios for the reaction
$Li^7 + Cs^{133} \rightarrow Ce^{137,137m} + 3n$, as a function of the excitation
energy. The upper scale shows the laboratory energy of the pro-
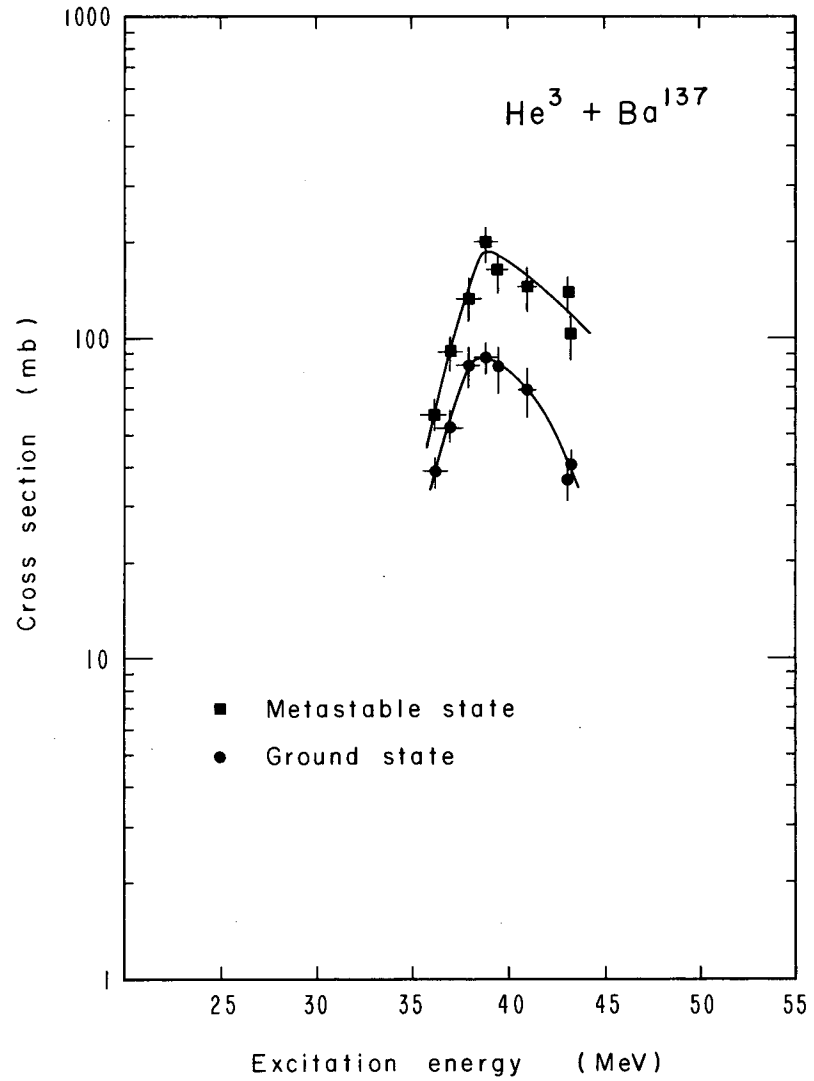jectile. The solid line connects the points.
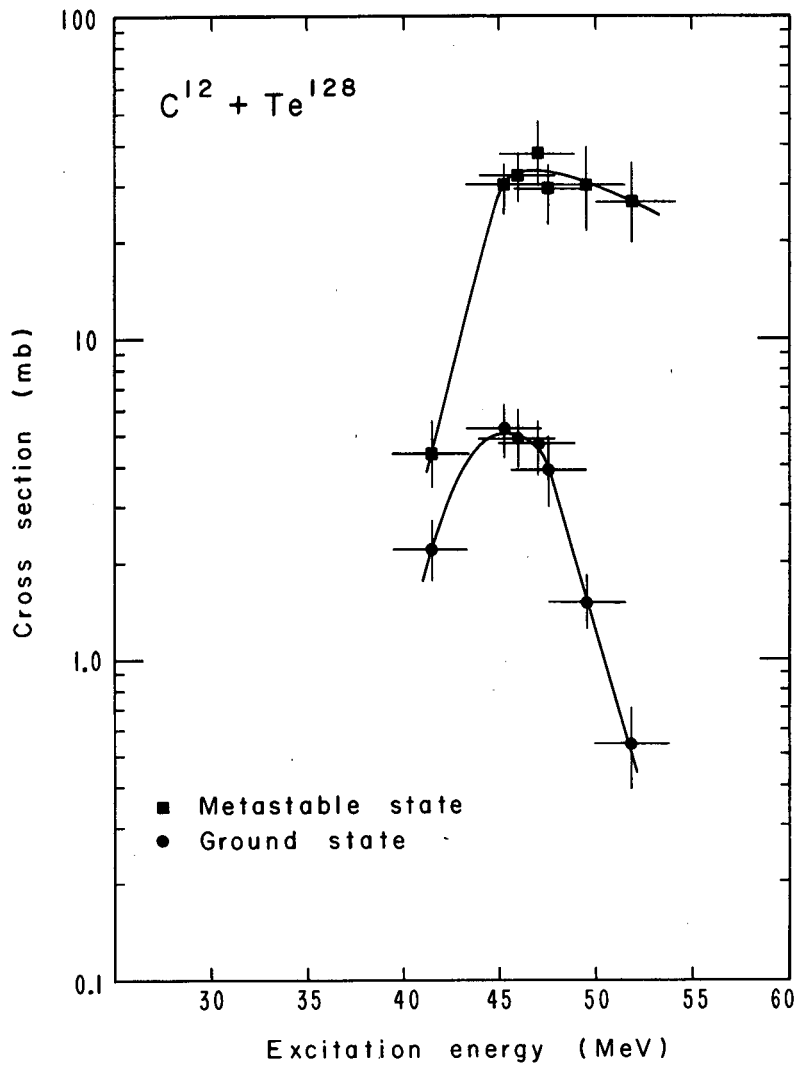
Fig. 10. The cross section as a function of the excitation energy for the reaction He⁴ + Ba¹³⁶ → Ce¹³⁷,¹³⁷ᵐ + 3n.

Fig. 11. The cross section as a function of the excitation energy for the reaction $He^3 + Ba^{137} \to Ce^{137,137m} + 3n$.

Fig. 12. The cross section as a function of the excitation energy for the reaction $C^{12} + Te^{128} \rightarrow Ce^{137,137m} + 3n$.

MU-32218

MU-32219

Fig. 13. The cross section as a function of the excitation energy for the reaction $Li^7 + Cs^{133} \rightarrow Ce^{137,137m} + 3n$.

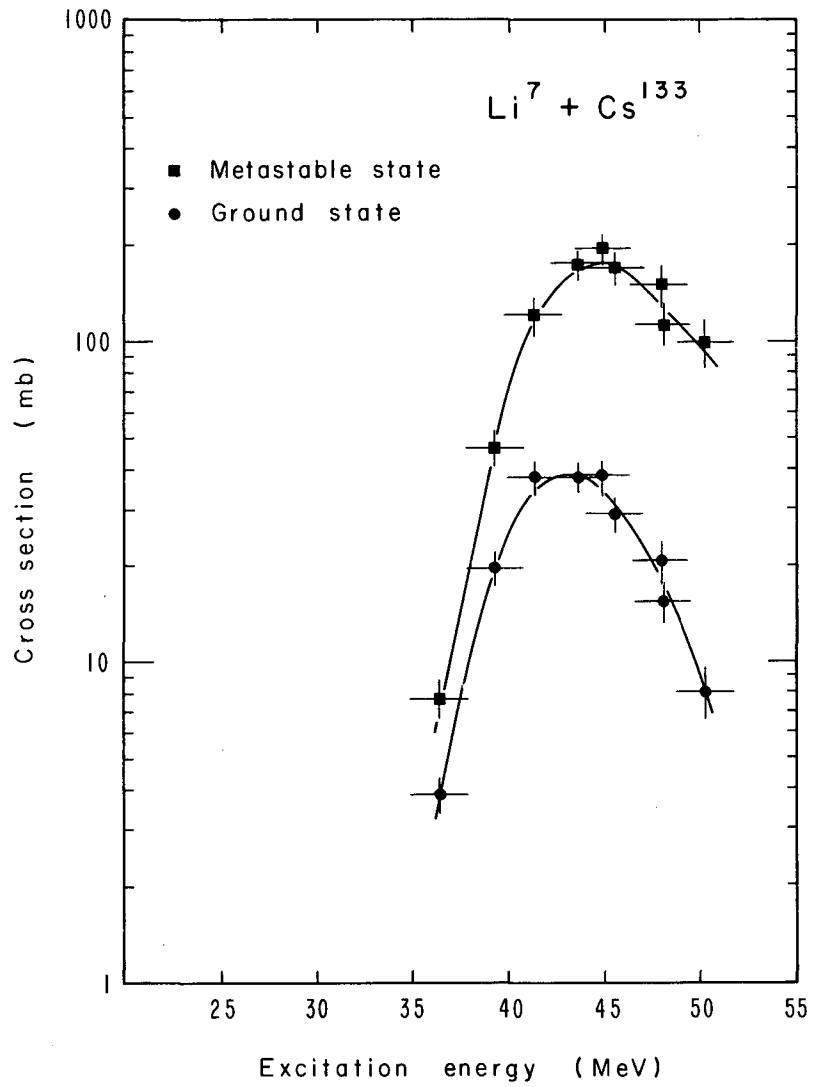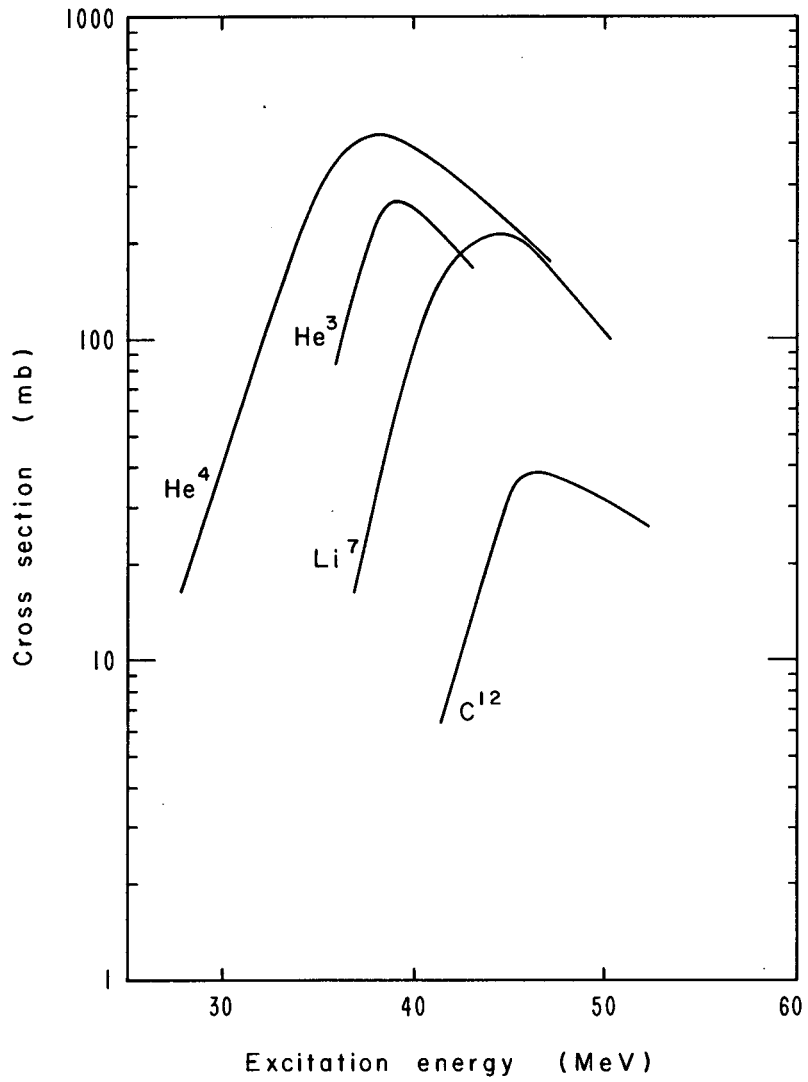Fig. 14. The combined metastable and ground-state cross sections
for all of the reactions as a function of the excitation energy

Table V. The Coulomb barrier and the reaction thresholds
for the systems studied.

Reaction		Coulomb barrier (MeV)		Reaction threshold (MeV)	
		E_{lab}	E^*	E_{lab}	E^*
$He^4 + Ba^{136} \rightarrow$	$Ce^{137} + 3n$	16.4	17.4	25.3	26.0
	$Ce^{136} + 4n$			33.2	33.7
	$Ce^{135} + 5n$	↓	↓	43.5	43.7
$He^3 + Ba^{137} \rightarrow$	$Ce^{137} + 3n$	16.6	31.9	10.6	26.0
	$Ce^{136} + 4n$			18.5	33.7
	$Ce^{135} + 5n$	↓	↓	28.7	43.7
$C^{12} + Te^{128} \rightarrow$	$Ce^{137} + 3n$	44.7	40.8	28.5	26.0
	$Ce^{136} + 4n$			36.9	33.7
	$Ce^{135} + 5n$	↓	↓	47.9	43.7
$Li^7 + Cs^{133} \rightarrow$	$Ce^{137} + 3n$	23.7	37.3	11.8	26.0
	$Ce^{136} + 4n$			19.9	33.7
	$Ce^{135} + 5n$	↓	↓	30.4	43.7

the ground state and metastable state had standard deviations associated
with them. The standard deviation of the ratio was calculated from the
expression

$$\sigma_Q = Q \ [(\sigma_1/R_1)^2 + (\sigma_2/R_2)^2]^{1/2} \ , \qquad (5)$$

where Q represents the ratio R_1/R_2 , and σ_1 and σ_2 are the standard
deviations of R_1 and R_2 .

For the Li^7 and C^{12} data, in which a graphical analysis was used,
the main error in the number of nuclei formed in the ground state represented
the limits within which a straight line could be extrapolated through the
data points to zero time. The errors in the number of nuclei formed in the
metastable state reflected the change in slope. The error in the ratio
was determined by using Eq. (5).

Errors in the individual data points come from two sources: the
random counting error and the error due to background subtraction. The
random error was usually 1 to 2%, but was never greater than 5%. Un-
certainties in the background subtraction were probably not greater than
10%. In most cases this would not affect the data point by more than 5%.
However, in a few of the points near the high-energy experimental limit,
this effect could be as large as 15% because the background is large com-
pared with the number of counts in the peak.

The vertical error bars indicated on the cross-section data points
are mainly due to the error in the number of nuclei present and to uncer-
tainties in the knowledge of the target thickness. The first of these has
been discussed above. The thickness of the Cs^{133} targets used in the Li^7
irradiations was probably known to within 5%. The Ba^{137} and Ba^{136} target
thicknesses were estimated to be known to within 10%. The thickness of
the Te^{128} targets was probably not known more accurately than to within
15%, because of electroplating difficulties discussed in Appendix A. Un-
certainties in the peak-to-total ratio, counter geometry, and counter
efficiency were probably not more than 3%. Calibration of the beam
integrator has shown that the value of the beam current is accurate to with-
in ± 3%.[29]

An additional uncertainty in the He^3 irradiations could arise because the Ba^{137} targets contained 17.4% Ba^{138}. The threshold for the reaction $He^3 + Ba^{138} \rightarrow Ce^{137m,137g} + 4n$ occurs at an excitation energy of 34.1 MeV. Since the target enrichment in Ba^{137} is 5 times that of Ba^{138}, it was estimated that the maximum contribution to the cross section from this effect was 5 mb. This is within experimental error.

The horizontal error bars on the cross-section points are due to the energy spread in the beam. This effect increases as the beam passes through degrading and target foils. The 60-inch cyclotron had an initial beam spread of about $\pm$ 1%. This was estimated to increase to $\pm$ 3% by the end of the foil stack. The Hilac also has an initial beam spread of about $\pm$ 1%. For the He^3 bombardments, this was estimated to increase to $\pm$ 3% by the end of the foil stack. The Li^7 and C^{12} irradiations would have a larger beam spread because they were both degraded to approximately half of their initial energy before striking the first target foil. Thus, we have estimated that the beam spread increases from $\pm$ 4% to $\pm$ 5% in the course of its passage through the foil stack.

D. Discussion

Figures 6 through 9 show that the variation of the isomer ratio with excitation energy is different for each of the reactions studied. This is more easily seen in Fig. 15, where all the experimental data are shown together. A strikingly similar picture results when the average angular momentum brought in by the projectile is plotted as a function of the excitation energy, as shown in Fig. 16. The implication that the variation of the isomer ratio with excitation energy is due primarily to the angular momentum is confirmed in Fig. 17, where a plot of the isomer ratio as a function of the average angular momentum is shown. At a given $\langle l \rangle$, where data overlap, the isomer ratios for the various reactions are all within experimental error of a common value. The calculation of $\langle l \rangle$ is discussed in Sec. IV.A.

When we compare isomer ratios resulting from different reactions, another consideration is the distance from the peak of the excitation function. Above the peak, where competition between the xn and $(x + 1)n$ reactions occurs, the xn reaction tends to proceed from the high-angular-momentum states. This condition arises because neutron emission lowers the excitation energy of the nucleus by about 10 MeV but does not remove more than 1 or 2 units of angular momentum, the emission of the extra neutron is hindered because the density of possible final states is low. Gamma-ray emission, which reduces the excitation energy by smaller amounts, is not hindered in this way. Thus, it can successfully compete with neutron emission even though neutron emission is energetically possible.[15] The systems with lower angular momentum tend to emit the extra neutron. Figure 18 shows that the isomer ratio at the peak of the excitation function for the various reactions varies in a linear manner with the angular momentum.
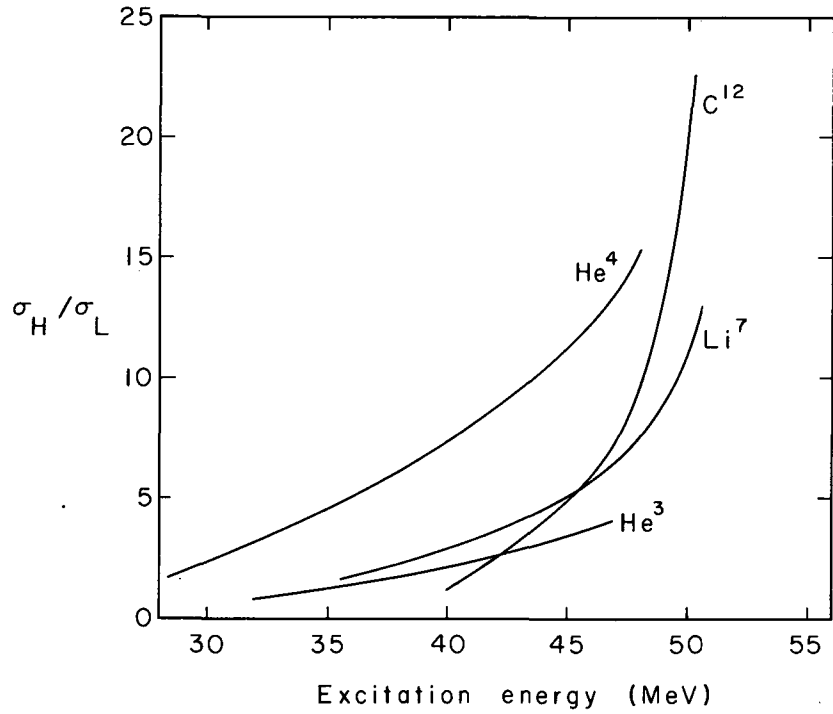
Fig. 15. The experimentally determined isomer ratios for all of the reactions studied as a function of the excitation energy.
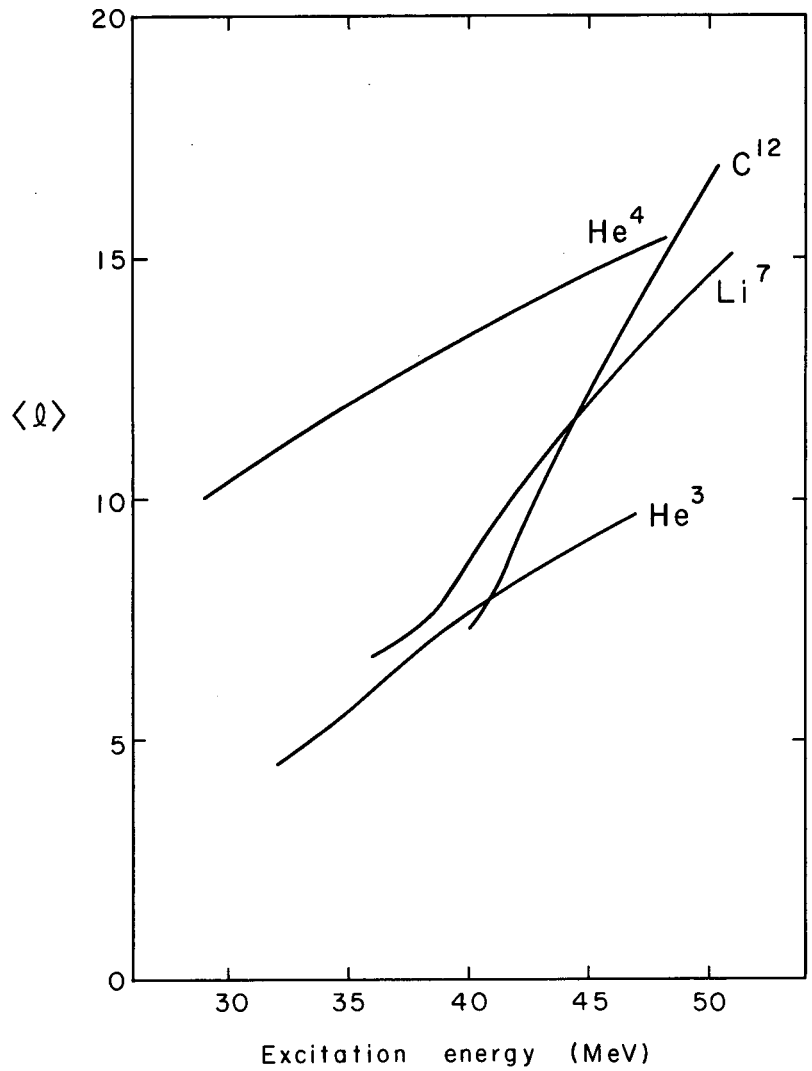
Fig. 16. The calculated average angular momentum as a function of the excitation energy for all of the reactions studied. The calculation of $\langle \ell \rangle$ is explained in the text.
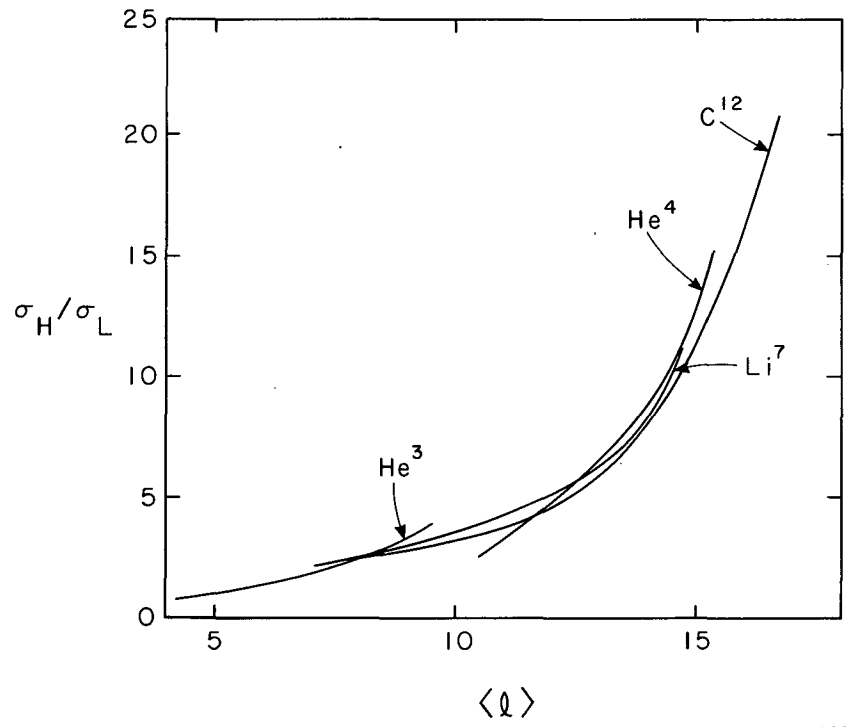
Fig. 17. The experimentally determined isomer ratios of all
of the reactions studied as a function of the average angular
momentum.
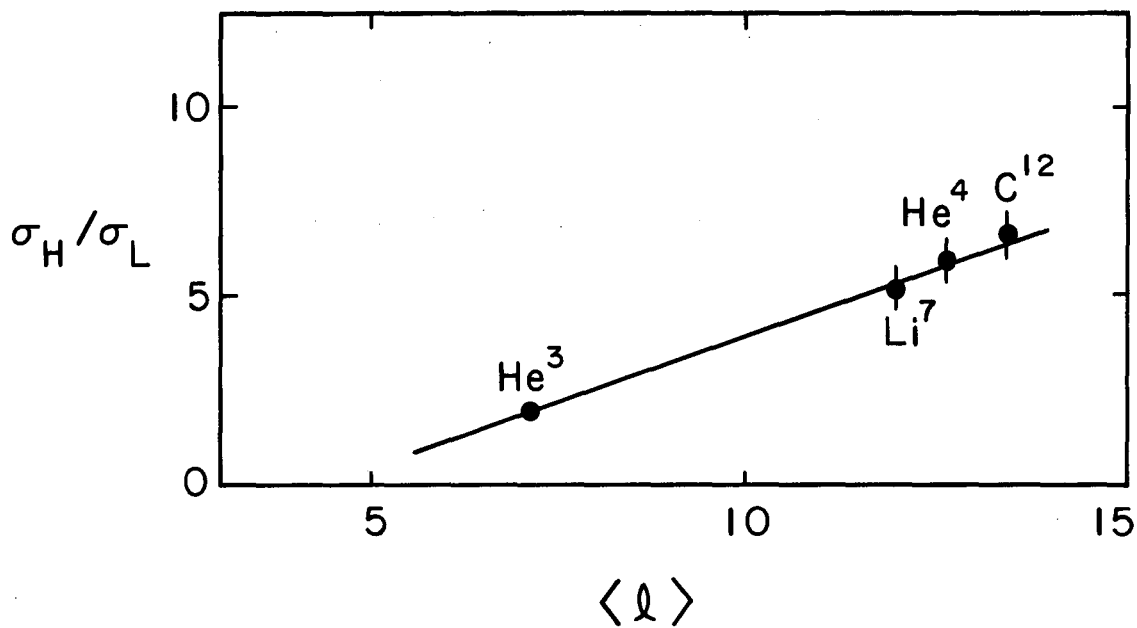
MU-32224

Fig. 18. The experimentally determined isomer ratio at the peak
of the excitation function for all of the reactions studied
as a function of the average angular momentum.

IV. CALCULATIONS

A. Calculation Procedures

The values of $\langle \ell \rangle$ for the He^4- and C^{12}- induced reactions were calculated by use of a computer program employing a parabolic approximation to the real part of the optical-model potential. The procedure has been described by Thomas.[31] The output of the program includes the transmission coefficients for a given ℓ value (T_ℓ), the total reaction cross section, and the average angular momentum. However, there is no provision for target and projectile spins. Thus, the $\langle \ell \rangle$ values for the Li^7- and He^3-induced reactions, in which the intrinsic spins are nonzero, were calculated from the first stage of the isomer-ratio calculation described by Hafner, Huizenga, and Vandenbosch.[32] The transmission coefficients, which were necessary for the input, were calculated with the parabolic approximation. The output includes the partial cross section (σ_j), and the probability of forming a state with a given J value (P_j). The average angular momentum is evaluated as

$$\langle J \rangle = \sum_{J=0}^{J=n} J_n P_{J_n} .$$

(8)

For the He^4 and C^{12} systems, this $\langle J \rangle$ was identical to the $\langle \ell \rangle$ of the parabolic calculation. For the Li^7 and He^3 reactions the $\langle J \rangle$ was approximately 5% higher than $\langle \ell \rangle$.

The parabolic approximation has been shown to be reasonably good above the Coulomb barrier. However, in the region of the barrier and below it the model becomes unsatisfactory.[33] Since we have compared the data at the peak of the excitation function, this model is probably sufficient to predict the average angular momentum.

Details of the parabolic approximation and isomer-ratio programs are shown in Appendix E.

B. Preliminary Calculation

If a sharp cutoff in the distribution of states of the compound
nucleus existed so that all the states with angular momentum below a cer-
tain value de-excited to the low-spin isomer while all those above went
to the high-spin isomer, the isomer ratio could be predicted by summing the
partial cross sections on both sides of the cutoff and dividing the low-
spin part by the high-spin part. An approach of this type by Katz et al.
was successful in predicting the ratio of isomers formed in some γ,n
reactions.[11] Seegmiller applied this method to a set of charged-particle
reactions and found that a specific cutoff gave a surprisingly good pre-
diction of the isomer ratio over a large energy region.[34] A similar
idealized calculation was performed for the reactions studied in this work.
The isomer ratio was calculated as

$$ R = \sum_{J=k}^{n} \sigma_J \Big/ \sum_{J=0}^{k} \sigma_J , \qquad (9) $$

where k is the cutoff point and n is the number of angular momentum
states in the compound-nucleus distribution. The calculated ratios for
different values of k are compared with the experimental values in Figs.
19 through 22. The peak of the excitation function is indicated by an
arrow in each of the figures. The experimental values rise more steeply
above the arrow than the calculated values in all reactions except those
induced by He^3. This is probably an effect of the competition between
neutron and γ-ray emission that causes the reaction to proceed from the
higher angular-momentum states. This effect will be noticeable only when
the high J values have appreciably large cross sections.

Below the peak of the excitation function, the reverse effect should
be noticed. However, in this region the Coulomb barrier begins to inter-
fere. The calculations are no longer valid for any of the reactions ex-
cept the one induced by He^4. In this case, the Coulomb barrier is suf-
ficiently low and the experimental values do drop off faster than those
which were calculated (see Fig. 19).
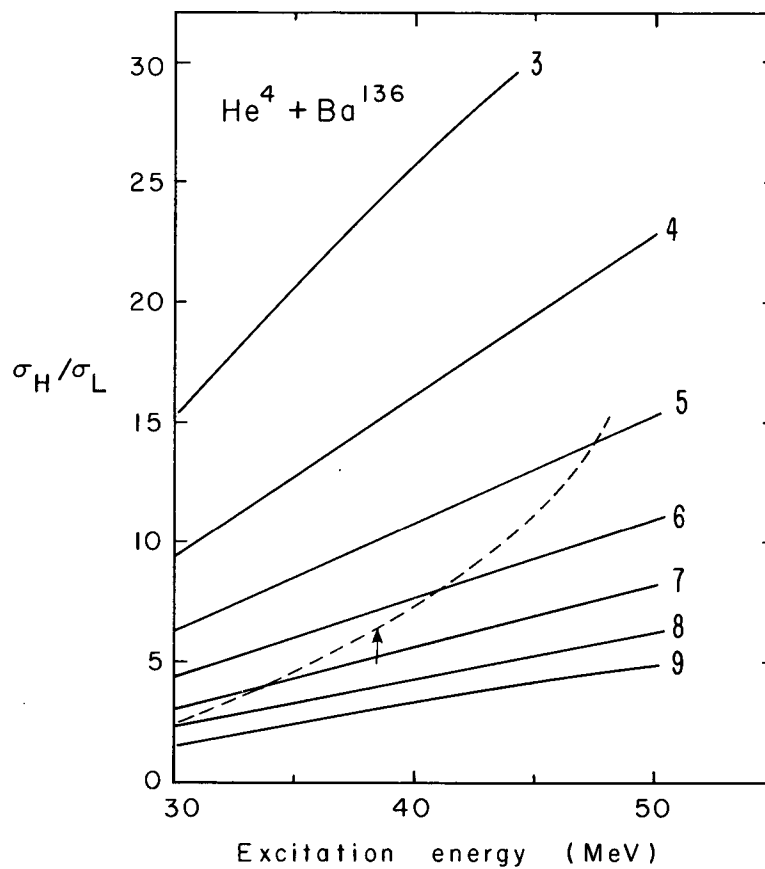
Fig. 19. The isomer ratio calculated according to Eq. (9) for the reaction $He^4 + Ba^{136} \rightarrow Ce^{137,137m} + 3n$, plotted as a function of the excitation energy. The lines are numbered according to the value of k used in the calculation. The dashed line represents the experimental values.
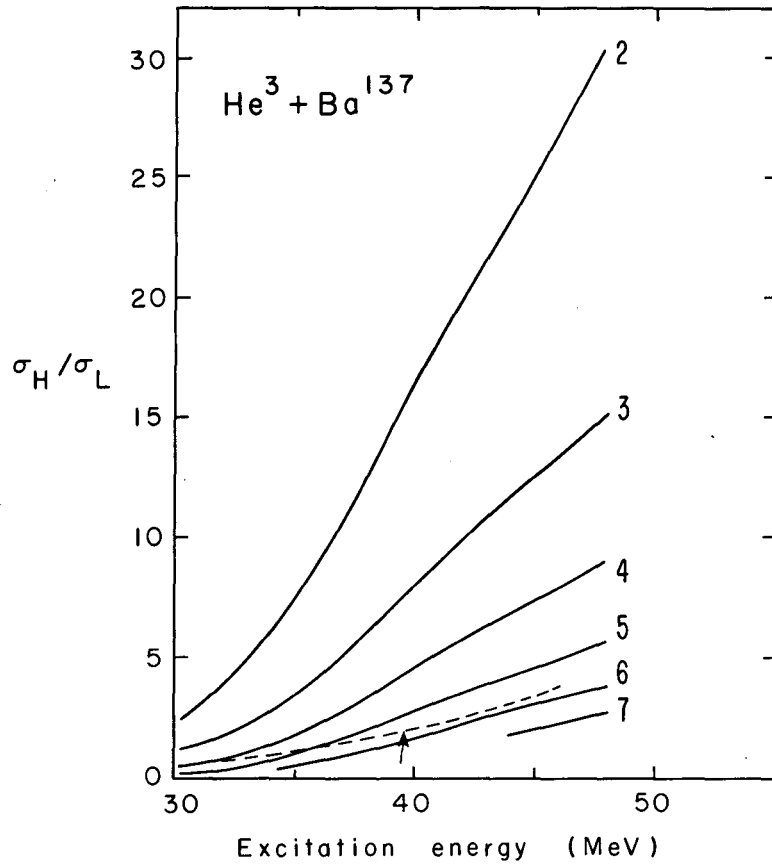
Fig. 20. The isomer ratio calculated according to Eq. (9) for the reaction $He^3 + Ba^{137} \rightarrow Ce^{137,137m} + 3n$, plotted as a function of the excitation energy. The notation is the same as for Fig. 19.

MU-32227

Fig. 21. The isomer ratio calculated according to Eq. (9) for the reaction $C^{12} + Te^{128} \rightarrow Ce^{137,137m} + 3n$, plotted as a function of the excitation energy. The notation is the same as for Fig. 19.
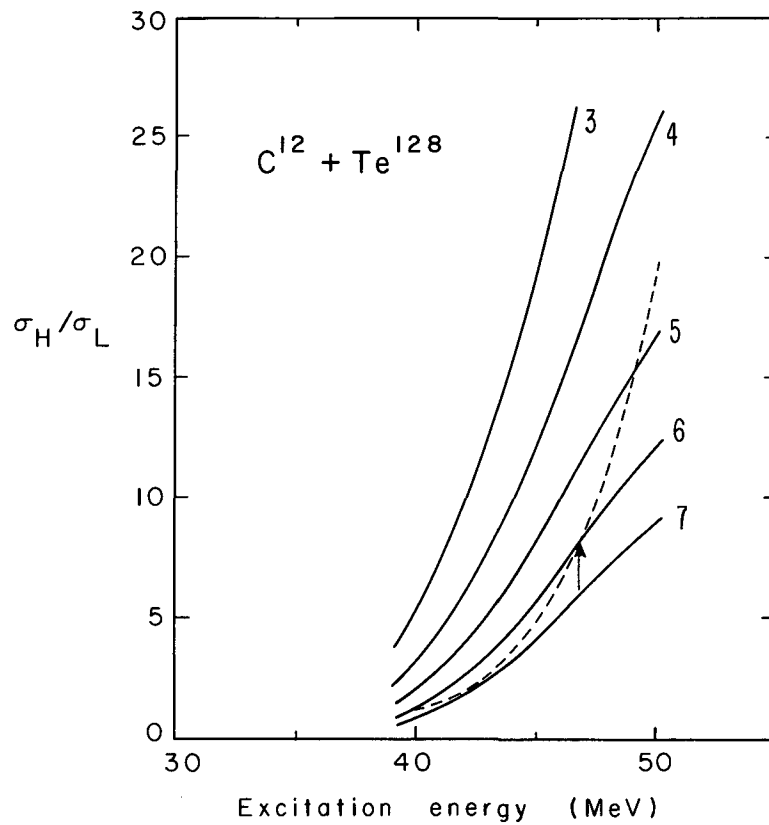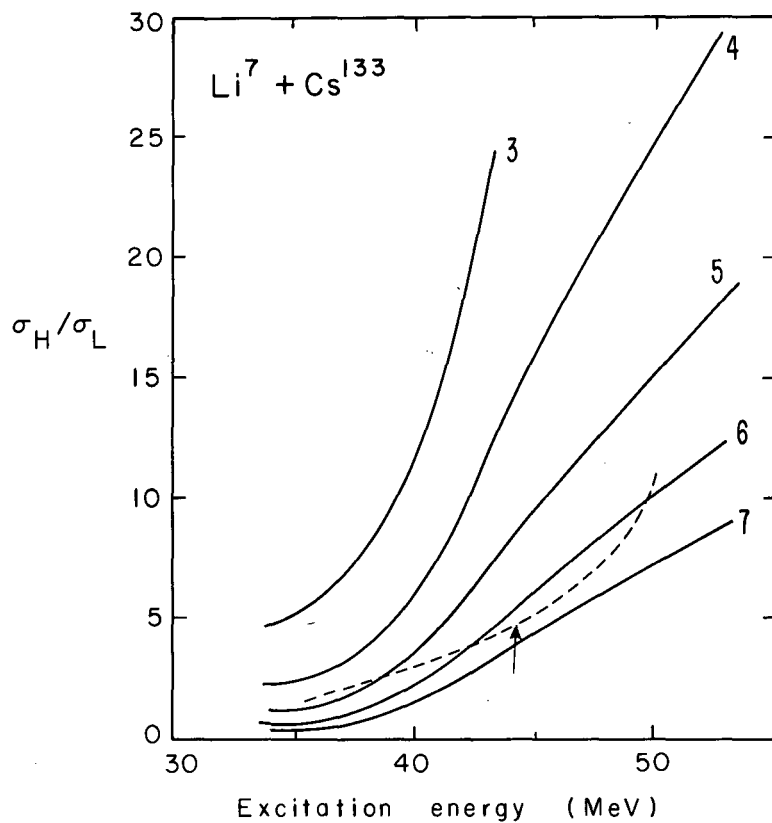
MU-32228

Fig. 22. The isomer ratio calculated according to Eq. (9) for the reaction $Li^7 + Cs^{133} \rightarrow Ce^{137,137m} + 3n$, plotted as a function of the excitation energy. The notation is the same as for Fig. 19.

The experimental isomer ratios at the peak of the excitation function fall between the calculated curves for k = 5 and k = 7 in all cases. It is interesting that the same cutoff region works for all the reactions even though there are different amounts of angular momentum in each one.

C. Isomer-Ratio Calculations

As indicated in Appendix E, the isomer-ratio program calculates the spin distribution for the excited compound nucleus and for each step in the de-excitation. Plots showing the change in distribution throughout the process are ahown in Fig. 23. The distribution resulting from the emission of the next-to-last γ ray in the cascade is used to determine the isomer ratio. The last γ ray is assumed to populate either the high-spin or low-spin isomer, depending upon which transition has the smaller spin change. The metastable state of Ce^{137} has a spin of 11/2- and the ground state has a spin of 3/2+ . Thus all states in the distribution with spins above J = 7/2 should populate the metastable state, whereas those states below it should populate the ground state. The state with J = 7/2 should be split between the two isomers if only spin were considered. However, recent work on the energy levels of Ce^{139}, which has an 11/2- metastable state and a 3/2+ ground state, showed that all the low-lying states (except for the isomeric state) had positive parities.[35] A state of spin and parity 7/2+ exists at 1.34 MeV. A similar situation probably exists for the low-lying levels of Ce^{137}. The transition from the 7/2+ state to the 3/2+ ground state is E2, whereas a transition to the 11/2- metastable state is M2. Since the electric quadrupole (E2) transitions occur much faster than those of magnetic quadrupole (M2) character, it was assumed for those calculations that the 7/2 state decayed entirely to the ground state.

1. Parameters Necessary for the Calculation

The results of the calculation are effected by the values given to various parameters. One of the more basic of these is the level-density
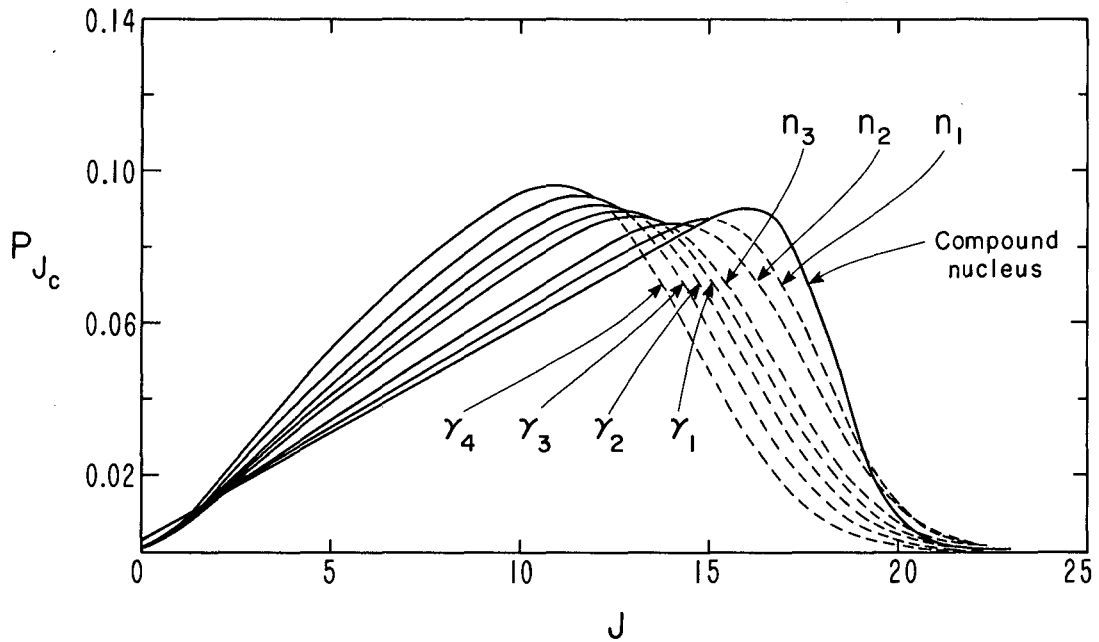
Fig. 23. The spin distribution at various stages in the compound
nucleus de-excitation plotted as a function of J. The curve
labeled n_1 represents the distribution after the emission of
one neutron. The other curves are labeled accordingly. The
distributions shown are for the reaction $He^4 + Ba^{136} \rightarrow Ce^{137,137m}$
+ 3n, at a bombarding energy of 35 MeV.

parameter $\underline{a}$. It arises in the level density formula[36] $\rho(A,E) = C \exp [2(\underline{a},E)^{1/2}]$, and is related to the single-particle level density g by the relationship[37]

$$\underline{a} = (1/6)\pi^2 g. \tag{10}$$

The approximate value of $\underline{a}$ has often been taken to be $(A/10)\text{MeV}^{-1}$.[38] Other analysis suggests $\underline{a} = A/8$ with lower values near closed shells.[39] Since Ce^{137} is three neutrons away from the 82-neutron shell, values of $\underline{a} = A/10$ and $\underline{a} = (A/8)\text{MeV}^{-1}$ were used. Figure 24 shows the effect of $\underline{a}$ on the calculation of the isomer ratio.

It was assumed that the energy carried off by the emitted neutrons was the average kinetic energy. This approximation has been found to be quite reasonable.[13] The values for the average energy were taken from the data of Simonoff and Alexander, who plot the average energy of emitted neutrons as a function of available energy per emitted neutron for a series of heavy-ion reactions producing dysprosium.[40] Their data indicate that the average energy is independent of the reaction. The isomer-ratio calculation using these data was found to be consistent with a similar calculation using the mean kinetic energy given by evaporation theory, $2 (\underline{a} E^*)^{1/2}$. Transmission coefficients for the outgoing neutrons were taken from Feld et al.[41]

Another parameter important to the calculation is the number of γ rays in the cascade. Strutinski has given an equation for the average number of γ rays for the case in which the fraction of excitation carried off by each photon is small.[42] This is written as

$$\tilde{N}_\gamma = [1/(\ell + 1)] (\underline{a} E^*)^{1/2} . \tag{11}$$

This same work also contains an equation for the average energy of the γ rays. This equation has been modified by Vandenbosch and Haskin so that for dipole radiation the γ rays have an average energy
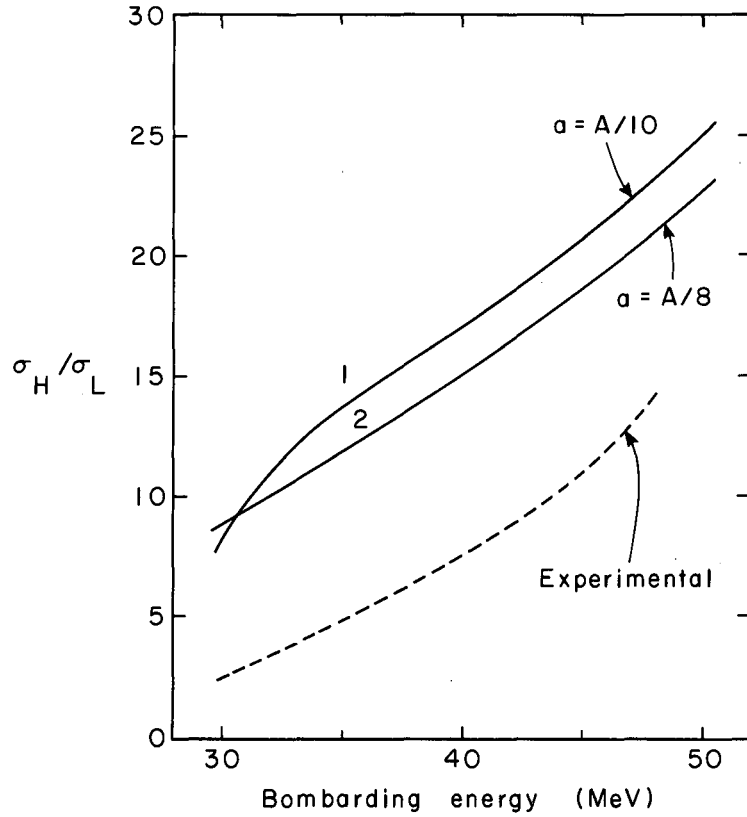
MU-32232

Fig. 24. Curves showing the effect of the level density parameter,
a, on the isomer-ratio calculation. The other parameters were
the same for both curves. The parameters are listed in Table
VI.

$$\tilde{E}_\gamma = 4[(E^* - 1)/\underline{a}]^{1/2} . \tag{12}$$

Mollenauer has found experimentally that the γ rays have an average energy of 1.2±0.3 MeV.[14] Each estimate was used in a calculation in which all the other parameters were the same. The results are shown in Fig. 25. It is seen that the three methods of evaluating the number of γ rays in the cascade give similar results. For a 45-MeV α particle incident on Ba^{136}, Eq. (11) predicts that seven γ rays are needed for the calculation, whereas Eq. (12) predicts six and the third estimate calls for nine γ rays. Since the gammas are of different energy, the results of the calculation are not appreciably changed.

Little is known about the multipolarity of the γ rays emitted. Mollenauer has found predominantly quadrupole radiation for He^4 bombardments of barium. However, for C^{12} incident on tellurium (a reaction that has more angular momentum), he found a predominance of dipole emission. Vandenbosch attributes most of the quadrupole radiation to the decay of states with very high angular momentum that were "forced" to get rid of it.[43] In spite of the higher multipolarity of the γ rays, these states will still eventually populate the high-spin isomer. Since the isomer-ratio calculation is dependent upon the low-lying states that could populate the low-spin isomer after γ-ray emission, he did not consider quadrupole radiation. In this work, one calculation was performed with quadrupole γ rays only. This is shown with a similar calculation using dipole γ rays only in Fig. 26.

The most sensitive parameter in the isomer-ratio calculation is σ, the spin cutoff parameter. Since the calculation is a statistical one, the dependence of the nuclear level density on the angular momentum is important. The nuclear level density has the approximate form[13]
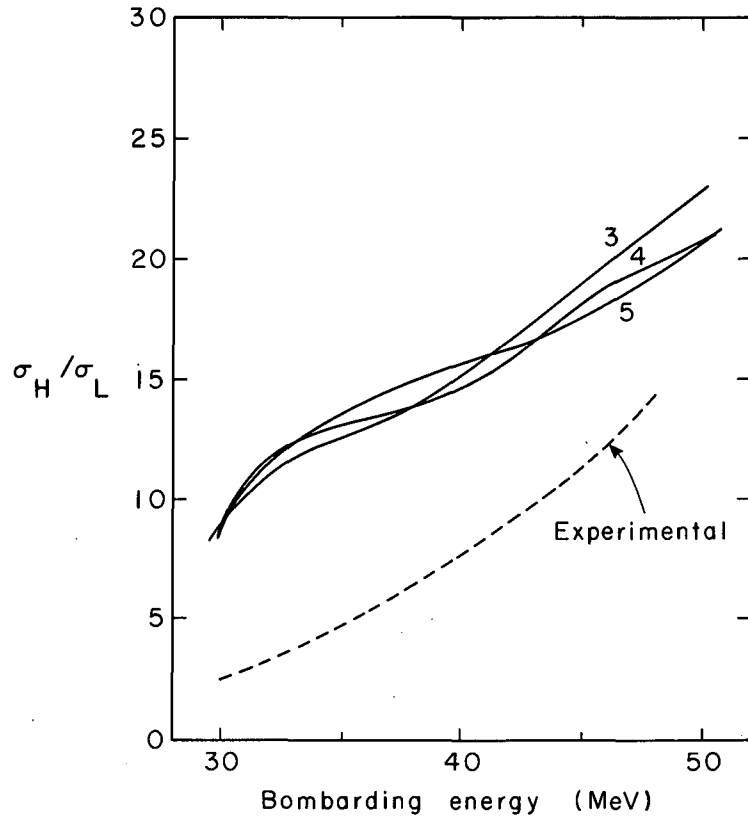
$$\rho(J) = \rho(0) (2J + 1) \exp[-(J + \tfrac{1}{2})^2/2\sigma^2], \tag{13}$$

Fig. 25. Curves showing the effect of the number of gamma rays in
the cascade on the isomer-ratio calculation. The calculation
of curve 3 employed Eq. (11), that of curve 4 used Eq. (12),
and the calculation of curve 5 assumed 1.2 MeV/γ. The other
parameters were the same for each curve.
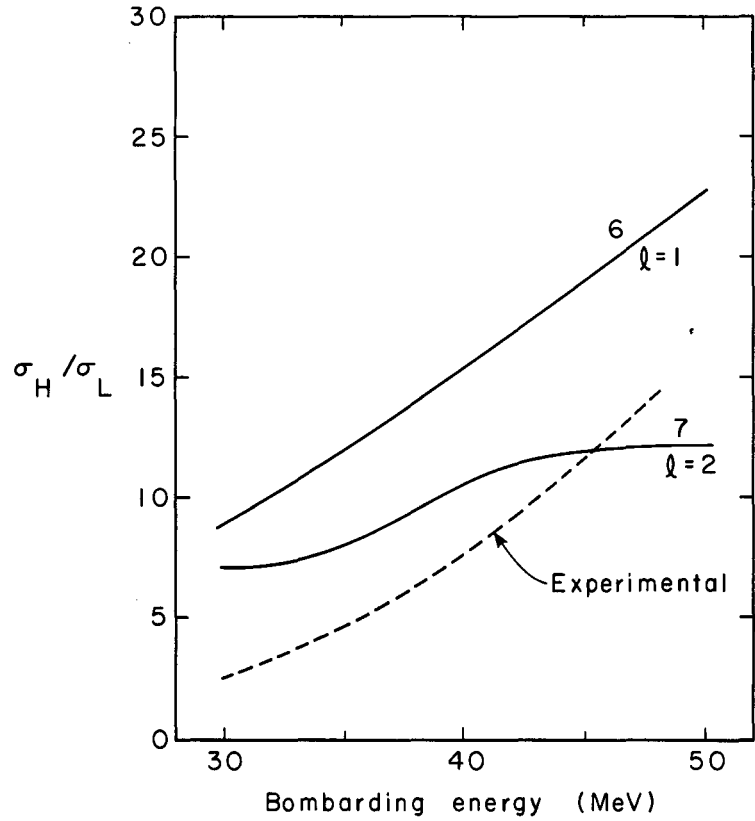
Fig. 26. Curves showing the effect of the multipolarity of the
gamma rays on the isomer-ratio calculations. The other param-
eters were the same for both curves.

where $\rho(0)$ is the density of levels with zero angular momentum and contains most of the level density dependence on excitation energy. The parameter σ , characterizes the distribution of J in the nuclear levels. Its value depends upon the choice of nuclear model. In the simplest case, the Fermi gas model,

$$\sigma^2 = c\ t = \mathcal{J}_r\ t/\hbar^2\ , \tag{14}$$

where $\mathcal{J}_r$ is the rigid-body moment of inertia. It has been shown that[44]

$$\mathcal{J}_r = (2/5)\ M_n R^2\ A\ , \tag{15}$$

where M_n is the nucleon mass and R is the nuclear radius taken as 1.2 $A^{1/3}$ fermis. The thermodynamic temperature t comes from the equation of state for this model,

$$E^* = \underline{a}\ t^2 - t\ . \tag{16}$$

The Fermi gas model has been shown to be valid at excitation energies of $\approx$ 10 MeV and above. However, below this energy, the moment of inertia is expected to be less than the rigid-body value.[45,46] This reduction has been attributed to the pairing interaction, which favors states with particles coupled in pairs to zero angular momentum. The Fermi gas model has been modified to include a simple form of pairing.[47,48] In this model, the energy required to break a pair of nucleons is 2δ and is taken to be independent of the excitation energy. The approximate equation of state becomes[48]

$$U = \underline{a}\ t^2\ \{0.25 + 0.75\ \exp(-0.874\delta/t)[1 + (0.874\delta/t)]\} - t, \tag{17}$$

where U is the excitation energy for an even-even nucleus, so that

$$U = E^* \qquad\qquad \text{even-even nuclei,}$$
$$U = E^* + \delta \qquad\quad \text{odd-mass nuclei,} \qquad\qquad (18)$$
$$U = E^* + 2\delta, \qquad\quad \text{odd-odd nuclei.}$$

The pairing energy is approximated by[49]

$$2\delta \approx 3.36 - 0.0084 \text{ A MeV.} \qquad\qquad (19)$$

The spin cutoff factor becomes

$$\sigma^2 = c''t , \qquad\qquad (20)$$

where

$$c'' = (c')^{1/3} (1/2\ c + 1/2\ c')^{2/3} \qquad\qquad (21)$$

and

$$c't = ct \exp(-0.874\delta/t) + \epsilon \langle m^2 \rangle [1 - \exp(-0.874\delta/t)] ,$$

$$(22)$$

where ϵ = 0, 1, or 2 depending upon whether the nucleus is even-even, odd mass, or odd-odd. The factor $\langle m^2 \rangle$ is the mean square value of the magnetic quantum number of individual nucleons and is taken equal to $\mathcal{I}_r/(\hbar^2 g)$.[50]

A third nuclear model pertinent to this work employs the Bardeen, Cooper, and Schrieffer theory of the superconducting state.[51] According to this theory, a transition temperature exists below which excitation of a given particle requires an energy (E_k) which is more than that required in the Fermi gas state (e_k). The energy difference is given by the expression $E_k^2 = e_k^2 + \theta^2$. The quantity θ has a value of θ_0 at a temperature very near zero, and diminishes to 0 at the transition temperature. The transition temperature t_c, is defined as 0.57 θ_0, and $\theta_0 \approx \delta$. Below the transition temperature, the approximate equation of state is[37]

$$E = \underline{a}\, t^2 \exp(-\theta/t)\, [1 + 2\theta/t + 2(\theta/t)^2]\, [1 + 2\theta/t]^{-1/2} - c\,, \qquad (23)$$

where

$$C = (1/4)g\, [\theta^2 - \theta^2 \ln(\theta^2/\theta_0^2) - \theta_0^2]\,.$$

The values of θ/θ_0 as a function of t/t_c are given in Ref. 49. The spin cutoff factor for this model becomes

$$\sigma^2 = c'''\, t = ct[2(1 + 2\theta/t)^{1/2}]\, [1 + \exp(\theta/t)]^{-1} + \epsilon\langle m^2\rangle[1 - \exp(-\theta/t)]\,. \qquad (24)$$

Above the transition temperature, the nucleus is expected to behave as a Fermi gas and obey the relationship

$$E^* = \underline{a}\, t^2 - t + (g/4)\delta^2 - \epsilon\delta\,. \qquad (25)$$

The spin cutoff factor is then given by Eq. (14). For Ce^{137} the transition temperature is 0.62 MeV. This corresponds to an excitation energy of 9.1 MeV.

The spin cutoff factor calculated for each of the three nuclear models is shown in Fig. 27 as a function of excitation energy. Figure 28 shows the effect of σ on the isomer-ratio calculations. The curves are labeled to indicate the method of calculation - σ_r for the Fermi gas model, σ_p for the simple pairing model, and σ_s for the superconductor model.

2. Results of the Calculation

Many calculations were performed with different combinations of the parameters described above. Figures 24, 25, 26 and 28 show the effect of these parameters on the calculation of the isomer ratio for the reaction $He^4 + Ba^{136} \rightarrow Ce^{137} + 3n$. Table VI lists the various parameter values used in each calculation. It is evident that the calculated values of the
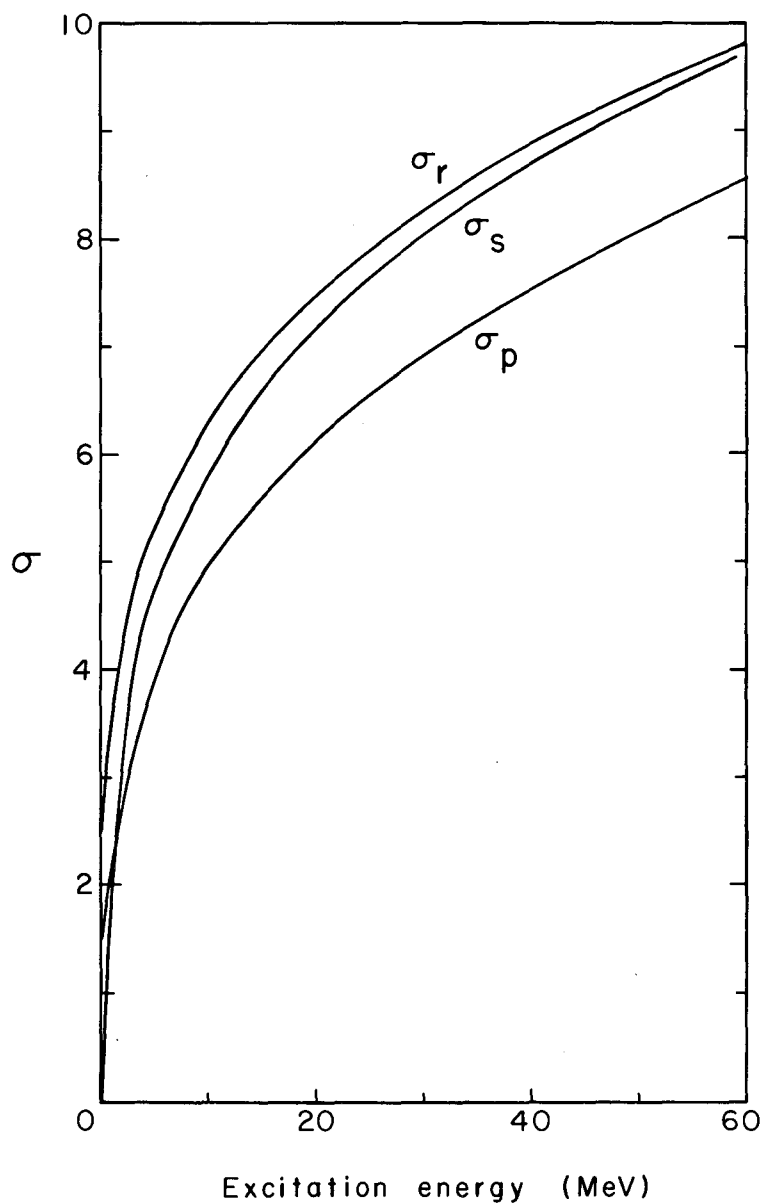
Fig. 27. The spin cutoff factor plotted as a function of excit-
tation energy. The different curves represent σ calculated
according to three nuclear models: the Fermi gas model (σ_r),
a simple pairing model (σ_p), and the superconductor model (σ_s).
In the latter two curves $\epsilon = 0$.
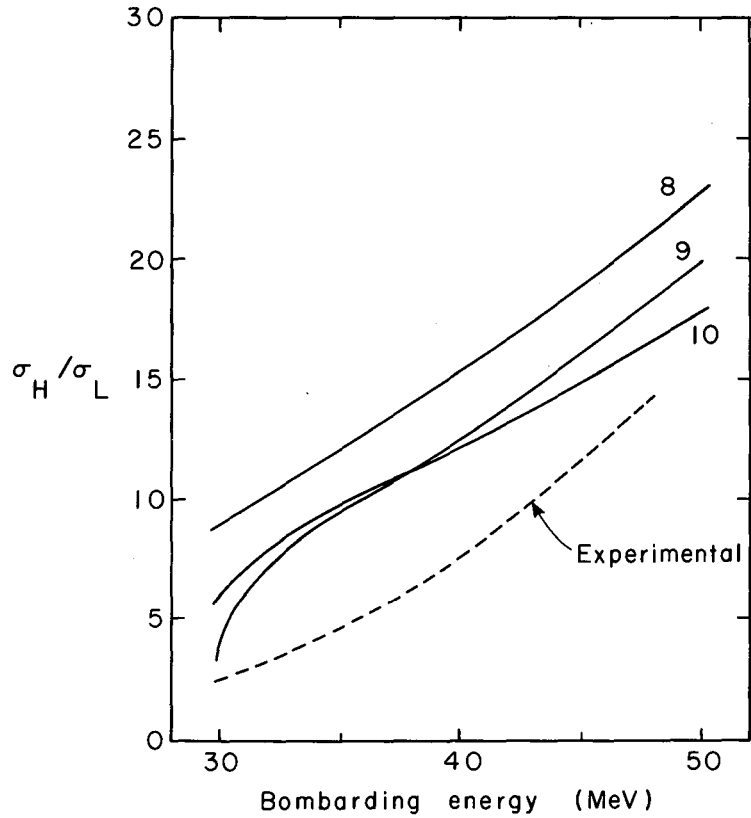
Fig. 28. Curves showing the effect of the spin cutoff factor on
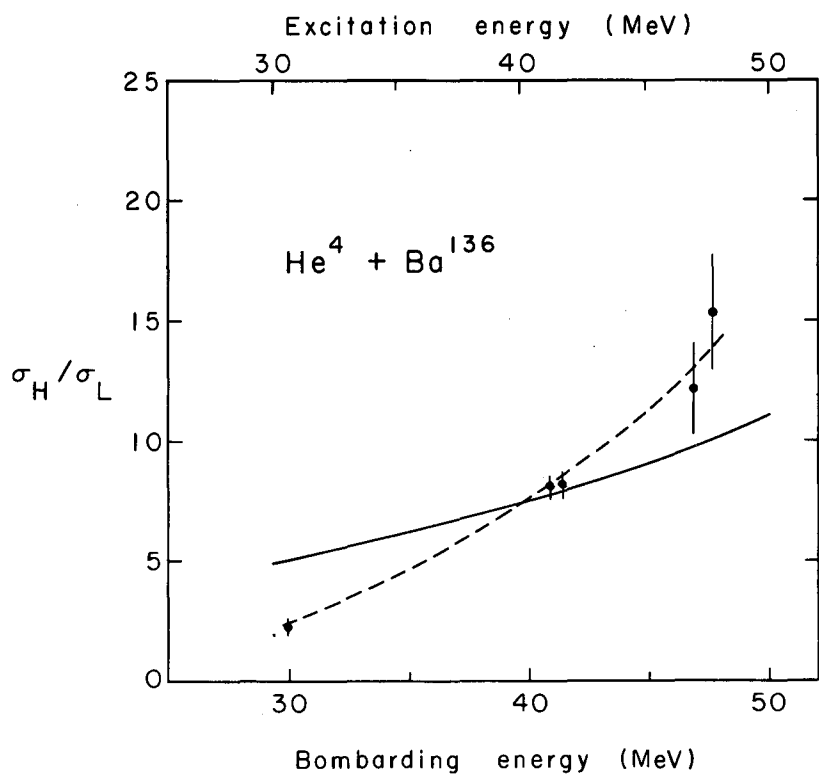the isomer-ratio calculations. The calculation of curve 8
employed the Fermi gas σ (σ_r), that of curve 9 used the super-
conductor σ (σ_s), and the calculation of curve 10 used the
pairing model σ (σ_p). The other parameters were the same in
each curve.

Table VI. Parameters used in the various calculations.

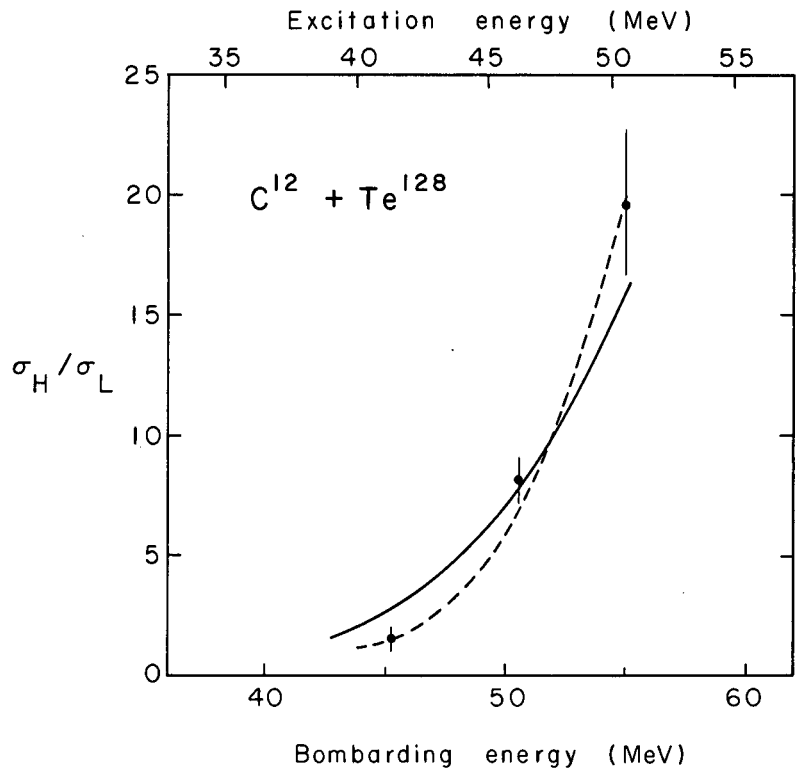| No.	Bombarding	$\underline{a}$	Equation used in calculating number of γ rays	Multipolarity of γ rays		Form of σ	Number of figure in which results shown
1	He^4	A/10	(11)	1		σ_r	24
2	He^4	A/8	(11)	1		σ_r	24
3	He^4	A/8	(11)	1		σ_r	25
4	He^4	A/8	(12)	1		σ_r	25
5	He^4	A/8	a	1		σ_r	25
6	He^4	A/8	(11)	1		σ_r	26
7	He^4	A/8	(11)	2		σ_r	26
8	He^4	A/8	(11)	1		σ_r	28
9	He^4	A/8	(11)	1		σ_s	28
10	He^4	A/8	(11)	1		σ_p	28
11	He^4	A/8	(11)	1	0.7	σ_r	29
12	C^{12}	A/8	(11)	1	0.7	σ_r	30
13	He^3	A/8	(11)	1	0.7	σ_r	31
14	Li^7	A/8	(11)	1	0.7	σ_r	32

[a] Value of 1.2 MeV/γ was used.

isomer ratio are too large when compared with the experimental values. Similar calculations for the C^{12}-, He^3-, and Li^7-induced reactions yielded results that are also too high. Apparently, the spin cutoff factor (σ) calculated according to each of the nuclear models is too large. Thus, a fraction of σ calculated according to the Fermi gas model was used to lower the results of the isomer-ratio calculations. The best fits were obtained when 0.7 σ_r was used. This corresponds to lowering the moment of inertia to 0.7 of the rigid-body value. The values calculated with 0.7 σ_r are compared with the experimental values for all the reactions studied in Figs. 21 through 32. Possibly other combinations of the parameters could also be found that would approximate the experimental results. However, since we did not know how accurate the estimates of the parameters were, we did not consider it worthwhile to pursue the problem further.

Fig. 29. A comparison of the experimental isomer ratios with the
isomer-ratio calculations by using 0.7 σ_r. The experimental
values are represented by the dashed line. The curves are for
the reaction $He^4 + Ba^{136} \rightarrow Ce^{137,137m} + 3n$.

Fig. 30. A comparison of the experimental isomer ratios with the
isomer-ratio calculation by using 0.7 σ_r. The experimental
values are represented by the dashed line. The curves are for
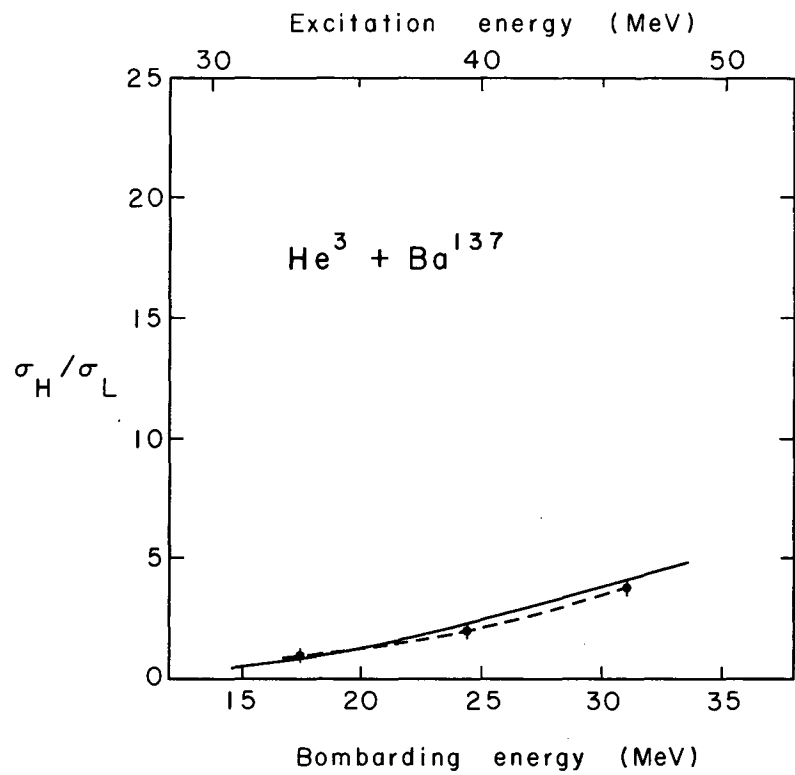the reaction $C^{12} + Te^{128} \rightarrow Ce^{137,137m} + 3n$.

Fig. 31. A comparison of the experimental isomer ratios with the
isomer ratios calculated by using $0.7 \, \sigma_r$. The experimental
values are represented by the dashed line. The curves are for
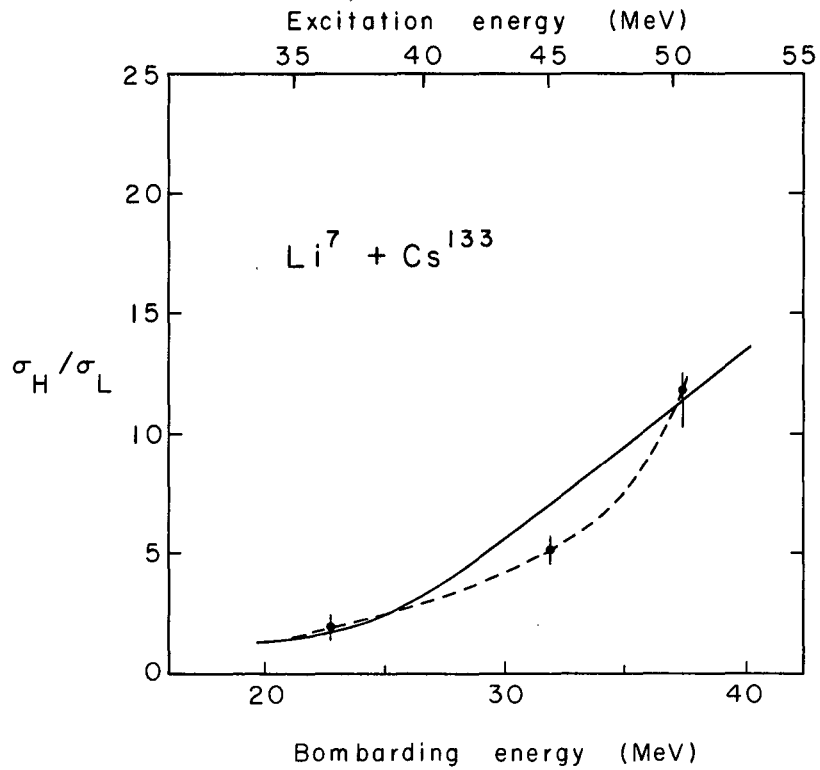the reaction $He^3 + Ba^{137} \rightarrow Ce^{137,137m} + 3n$.

Fig. 32. A comparison of the experimental isomer ratios with the
isomer ratios calculated by using 0.7 σ_r. The experimental
values are represented by the dashed line. The curves are for
the reaction $Li^7 + Cs^{133} \rightarrow Ce^{137,137m} + 3n$.

V. CONCLUSIONS

The experimental results lead to several conclusions:

1. The ratio of the formation cross section of the high spin isomer to that of the low-spin isomer increases with increasing bombarding energy.

2. The increase of the isomer ratio with energy is mainly due to the increase of the angular momentum with energy.

3. It is best to compare isomer ratios produced in different reactions at the peak of the excitation function. Above the peak, the isomer ratio is further increased by the competition of neutron and γ -ray emission that forces the reaction to proceed from states with high angular momentum. Below the peak, the reverse effect prevails and the reaction proceeds from low angular momentum states.

The calculations based on the theory of Huizenga and Vandenbosch show that with present knowledge of the various parameters, this formalism is adequate to describe the de-excitation of a compound nucleus to one of two long-lived nuclear states. Further information is needed on the level-density parameter $\underline{a}$, the number and multipolarity of γ rays, and the energy dependence of the spin cutoff factor before the theory can be completely tested.

ACKNOWLEDGMENTS

I wish to thank Professor Kenneth Street who suggested this problem and guided the course of this research.

To Drs. Victor Viola, John Alexander, and H. Marshall Blann, I am indebted for many valuable suggestions and encouragement.

I have appreciated many stimulating discussions with Dr. David Seegmiller and Mr. Paul Croft.

For the use of the isomer-ratio program, I thank Dr. Robert Vandenbosch of the Argonne National Laboratory.

The assistance of the accelerator crews and the Health Chemistry group is gratefully acknowledged.

I wish to thank my wife, Sharon, whose help in typing the various drafts of this thesis is sincerely appreciated.

A fellowship from the Woodrow Wilson Foundation provided financial support during the early part of this project.

This work was performed under the auspices of the U. S. Atomic Energy Commission.

APPENDICES

A. Target Preparation

1. Ba^{137}

Ba(NO$_3$)$_2$, enriched to 81.9% in Ba^{137}, was dissolved in a minimum amount of water and added to an equal volume of acetone. One-half-mil Cu foils were washed with water and acetone, heated at 600°F for 5 min, cooled, and weighed. The Ba(NO$_3$)$_2$ solution was brushed on and the foils were heated again. After cooling, they were lightly wiped with tissue paper and more solution was brushed on. The process was repeated about 15 times to get target foils that were 0.35 mg/cm^2 in Ba^{137}(NO$_3$)$_2$.

2. Ba^{136}

One-mil Cu foils were washed with water and acetone, placed in a furnace at 900°F for 15 min, cooled, and weighed. A water-acetone solution of Ba(NO$_3$)$_2$, enriched to 92.9% in Ba^{136}, was applied to the foils with a 250-λ micropipet. Four applications were made with alterante drying to produce foils that were 0.7 mg/cm^2 in Ba^{136}(NO$_3$)$_2$. Because the He^4 beams had to be kept so low, these targets were made thicker than those of the Ba^{137}.

3. Cs^{133}

A small dish made of 3-mil Ta foil was suspended between the electrodes of a vacuum evaporator and filled with CsNo$_3$. A 0.2-mil Cu foil was suspended above the dish by a tripod stand. An aluminum plate with a 0.75-in. hole in it was placed in front of the Cu foil so that a deposit of known area could be obtained. At a pressure of 10μ, the current was turned on and the dish heated to redness for 10 min. The resulting foils had CsNO$_3$ deposits whose thickness averaged 1 mg/cm^2.

This method produced the best target foils, but since it wastes much of the material it could be used only for the cesium targets in which Cs^{133} is the only stable isotope.

4. $\underline{Te^{128}}$

Tellurium metal, enriched to 96.4% in Te^{128}, was dissolved in 9 M HNO_3 and evaporated to dryness. The white flaky residue was dissolved in enough 0.2 $\underline{M}$ HNO_3 to make a plating solution 1 mg/ml in Te^{128}. Copper foil 0.05 mil thick was clamped between the brass base and Teflon cylinder of the plating cell, and the cylinder was filled with solution. A current between 2 and 3 mA was applied for 30 min. The weight of the Te^{128} plate seemed very small; this was not understood until it was discovered that the dilute nitric acid plating solution was attacking the Cu foils. A plain 0.2 $\underline{M}$ HNO_3 solution was applied to 0.05-mil Cu foils under identical conditions so that the amount dissolved could be determined and a correction be made to the foil weights.

The isotopic abundances of the various target materials are shown in Table A-I.

B. Range-Energy Relationships

Most of the range-energy relationships used in this work were taken from the literature.[21,52,53] However, the range of Li^7 in copper and cesium and the range of C^{12} in tellurium have not been tabulated. The range of a particle in a given material is related to that of a proton in the same material by

$$ R_i(T_i) = (1/z_i^2)(\mu_i/\mu_p) \, R_p \, [(\mu_p/\mu_i)T_i \,] \, , \tag{26} $$

where z_i is the charge of the particle, μ_i is its mass, μ_p is the mass of the proton, and $R_p[(\mu_p/\mu_i)T_i]$ is the range of a proton of energy $(\mu_p/\mu_i)T_i$. Since data for protons in cesium and tellurium were not available, the ranges of Li^7 in barium and C^{12} in iodine were calculated.

Equation (26) represents an approximation, since there is a slight dependence of the maximum energy transfer on μ_i. To correct for this, the range of Li^7 in aluminum was calculated with the proton data of Sternheimer[54] and divided into the values calculated by Northcliffe.[53]

Table A-I. The isotopic abundances of the target materials

| Target enriched in	Isotope	Abundance (%)	Target enriched in	Isotope	Abundance (%)
Ba^{136}	130	< 0.05	Te^{128}	120	< 0.05
	132	< 0.05		122	< 0.05
	134	< 0.1		123	< 0.05
	135	1.08 ± 0.05		124	< 0.05
	136	92.9 ± 0.1		125	0.06
	137	1.77 ± 0.05		126	0.77 ± 0.05
	138	4.24 ± 0.05		128	96.43 ± 0.1
				130	2.74 ± 0.1
Ba^{137}	130	< 0.03			
	132	< 0.03	Cs^{133}	133	100
	134	< 0.05			
	135	< 0.1			
	136	0.63 ± 0.05			
	137	81.9 ± 0.1			
	138	17.4 ± 0.1			

The quotient was used to correct the ranges in copper and barium. These ranges were calculated with the proton data of Sternheimer for copper and those of Williamson for barium.[21] The results are shown in Fig. 33.

In a similar way, the range of C^{12} in iodine was calculated by use of the proton data of Williamson, and corrected to the data of Hubbard. The results are shown in Fig. 34. Figures 35 and 36 show the range-energy data for He^3 and He^4 that are tabulated in Rev. 21.

C. Chemical Separation

The chemical procedure used was based on a separation described by Glendenin.[23] Each target foil was dissolved in 4.5 ml of 15 $\underline{M}$ HNO_3 to which was added 2 ml of 2 $\underline{M}$ $NaBrO_3$ and 1 ml of Ce^{+3} carrier solution (10 mg/ml). The cerium was oxidized to the +4 state by the $NaBrO_3$ and strong acid. The solution, which was 9 $\underline{M}$ in HNO_3, was transferred to a separatory funnel containing 15 ml of methyl isobutyl ketone (hexone). Before the chemistry was started, the hexone was equilibrated with an equal volume of 9 $\underline{M}$ HNO_3 to oxidize any reducing agents. The solution was shaken with two separate volumes of hexone and discarded. The two organic phases containing the yellow Ce^{+4} were combined and washed with 10 ml of 9 $\underline{M}$ HNO_3. The cerium was reduced and back-extracted into 5 ml of H_2O containing a few drops of a 30% solution of H_2O_2. The aqueous phase was removed, neutralized with NH_4OH, and acidified with 1.5 ml of 6 $\underline{M}$ HNO_3. This solution was heated to boiling, added to 15 ml of saturated $(NH_4)_2C_2O_4$, and cooled in an ice bath. The precipitate $[Ce_2(C_2O_4)_3 \cdot 9 H2O]$ was filtered on glass-fib r filter disks, washed with water, alcohol, and ether, then dried in a vacuum desiccator. After weighing, the filter disks were mounted on aluminum counting plates and covered with Scotch tape.

In order to determine the chemical yield of the samples, a known volume (1 ml) of a calibrated carrier solution (10.6 mg/ml) was always used in the chemical separations. As some doubt exists about the number of water molecules attached to each cerium oxalate molecule, the molecular weight of the oxalate precipitate could not be calculated. Thus some
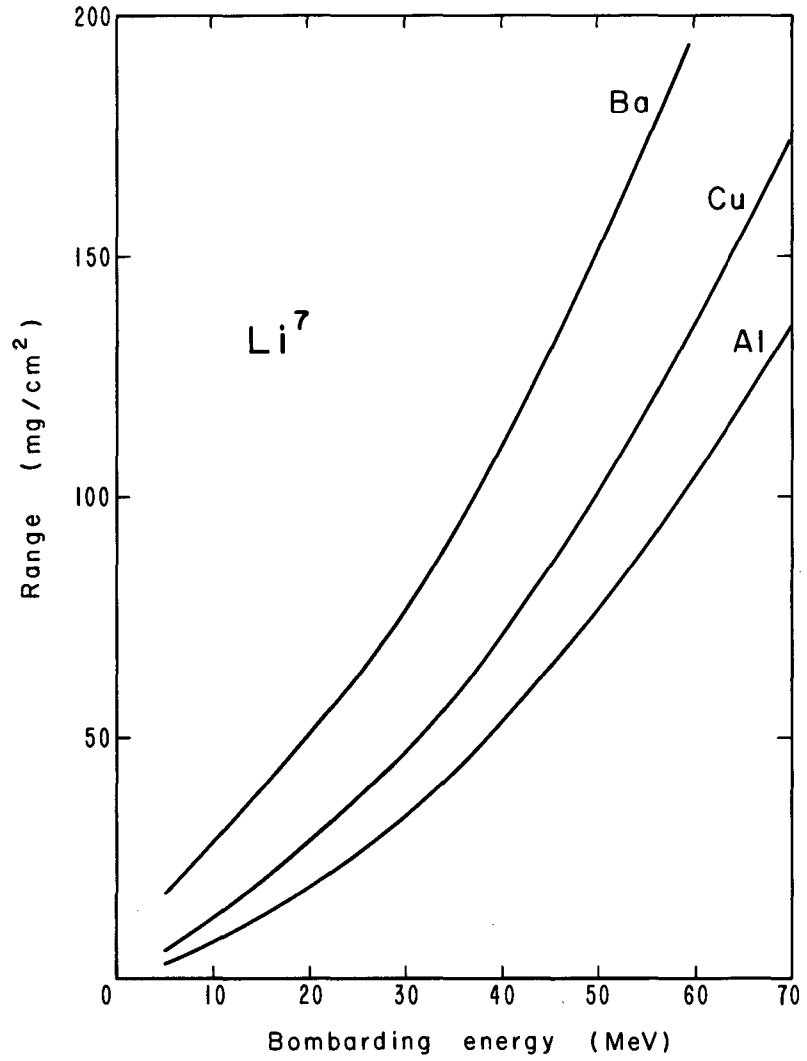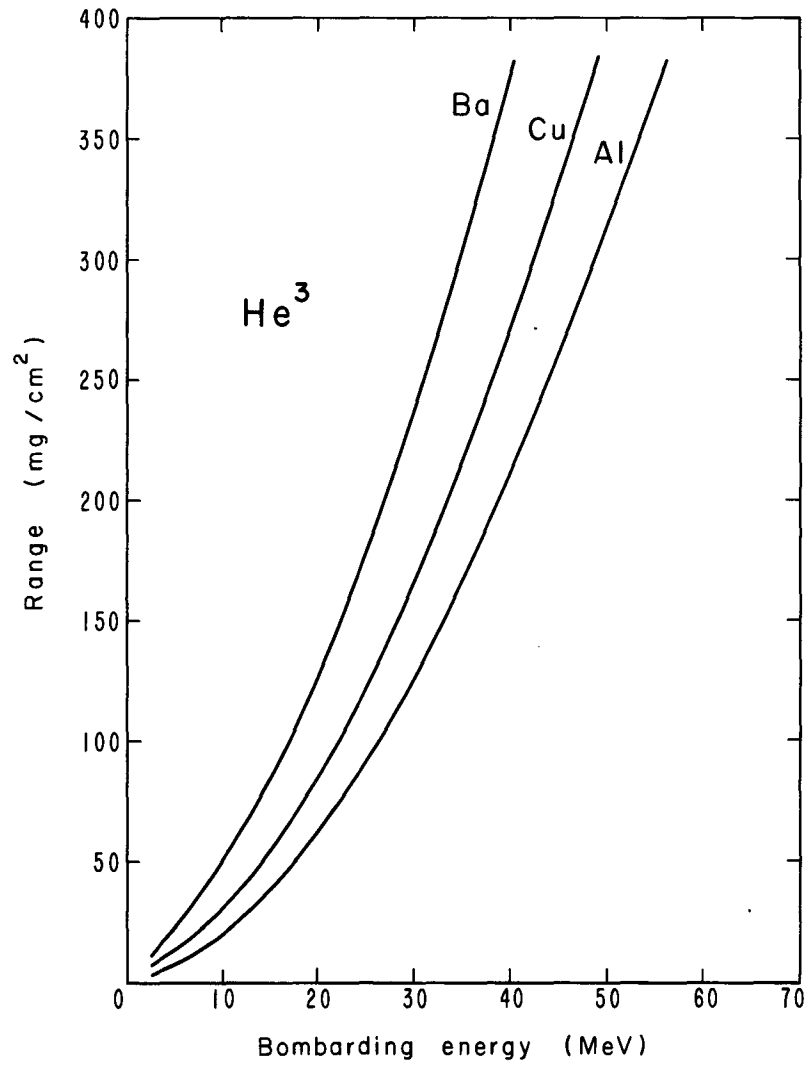
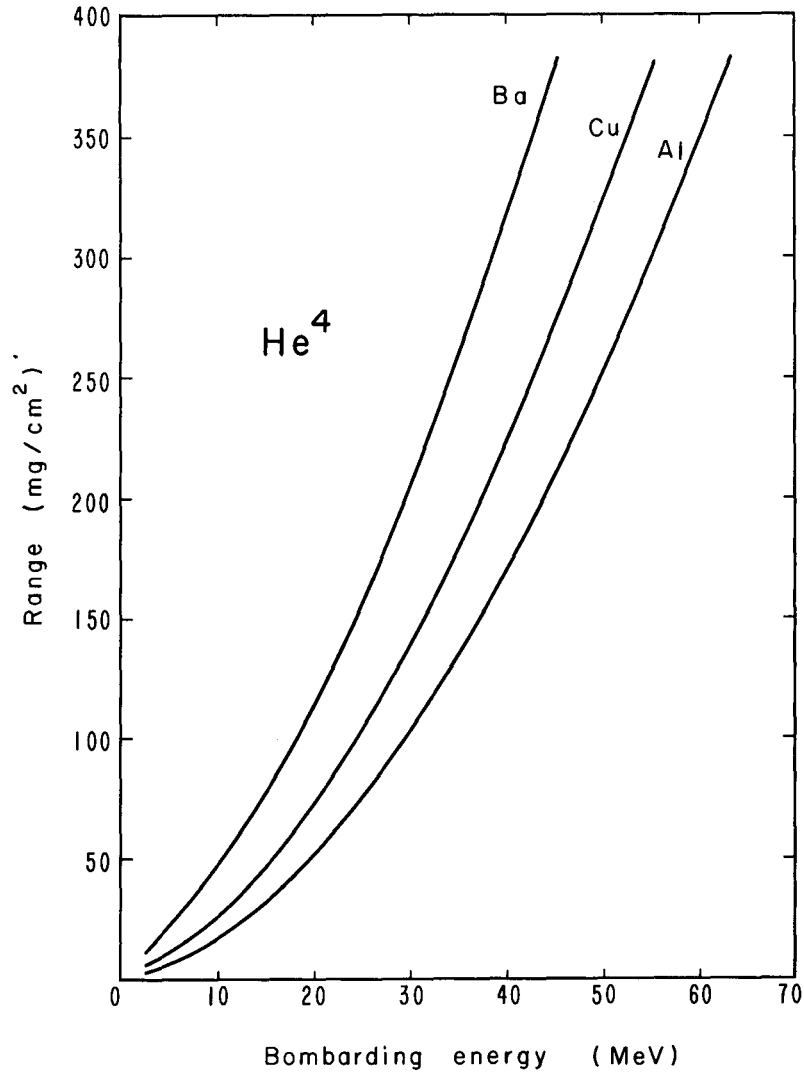Fig. 33. The range-energy relations for Li^7 in several materials.

C^{12}
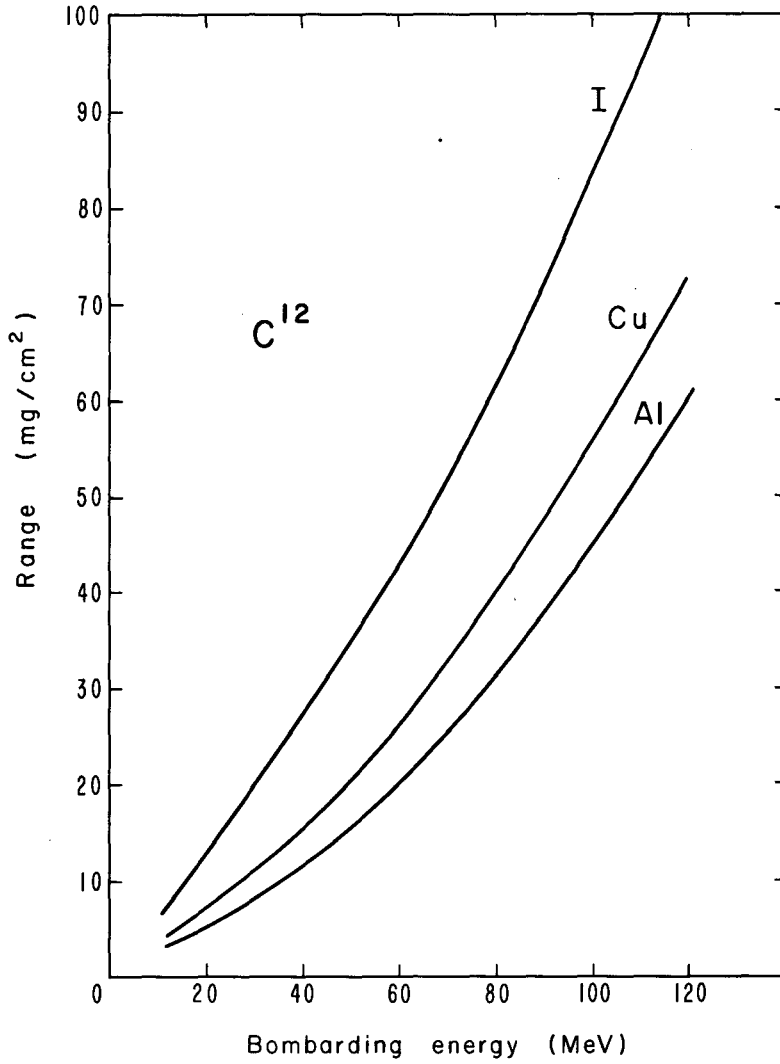
MU-32241

Fig. 34. The range-energy relations for C^{12} in several materials.

Fig. 35. The range-energy relations for He³ in several materials.

Fig. 36. The range-energy relations for He^4 in several materials.

nonradioactive samples were made in the usual way except that "ashless" filter paper was used in place of glass fiber filters. The oxalate precipitates were weighed, placed in tared crucibles, and ignited at $950^\circ C$ for 15 min to convert the cerium oxalate to cerium oxide (CeO_2). The amount of cerium present was determined from the weight of CeO_2. Since the amount of carrier used was known, the yield in these samples was established. By comparing the yield with the corresponding weight of the oxalate precipitate for each sample, the best value for the amount of precipitate formed in a separation with 100% chemical yield was determined. This value was determined independently of the number of water molecules attached to the precipitate, though a comparison of the weight of CeO_2 to that of the oxalate in the above samples showed that this number was 9.

D. Decay during Bombardment and Counter Geometry

The total number of nuclei (N_T) produced during irradiation for time T is related to the number present at the end of bombardment (N_0) by

$$N_T = N_0 \ (T/T_{1/2})\{0.693/[1 - \exp(- \lambda T)]\} \ . \tag{27}$$

For an isomer ratio, this expression becomes

$$N_{T_m}/N_{T_g} = (N_{0_m}/N_{0_g})(T_{1/2 \ g}/T_{1/2 \ m})\{[1 - \exp(-\lambda_g T)]/[1 - \exp(-\lambda_m T)]\} \ . \tag{28}$$

The uncorrected ratio of cross sections is N_{0_i}/N_{0_g}. Thus, the factor

$$(T_{1/2 \ g}/T_{1/2 \ i}) \ \{[1 - \exp(-\lambda_g T)]/[1 - \exp(- \lambda_m T)]\} \tag{29}$$

was multiplied by the experimental isomer ratios to obtain the corrected values. A plot of this factor as a function of time from the end of bombardment is shown in Fig. 37.

The geometry of the various shelves in the counter was determined by counting a Cs^{137} source whose disintegration rate was known. The area under the 662-keV peak was corrected for peak-to-total ratio,[25] and counter efficiency[55] to find the number of γ rays incident on the crystal. This number was divided by the disintegration rate to give the counter geometry. The results are shown in Fig. 38.

E. Computer Programs

1. Least-Squares Programs, FRENIC and LENIC

The FRENIC program performs an iterative least-squares analysis on a radioactive decay curve of as many as ten components. Thus, where y_i represents a measured data point at t_i minutes from the end of bombardment, a_j represents the ordinate intercept of the $\underline{j}$th component, and λ_j represents its decay constant, FRENIC fits the expression

$$\sum_{i=1}^{n} W_i \left[y_i - \sum_{j=1}^{k} a_j \exp(-\lambda_j t_i) \right]^2 \qquad (30)$$

to each point and minimizes the square of the deviations. W_i is the weighting factor and can be 1, $1/y_i$, $(1/y_i)^2$, or a number arbitrarily chosen and punched on each data card. A W_i of $(1/y_i)^2$ representing equal statistics was used in this work. Guesses of the A_j and λ_j are part of the input and may either be held constant or varied. The output contains a listing of the parameter guesses, final least-squares answers, and the standard deviation of each parameter.
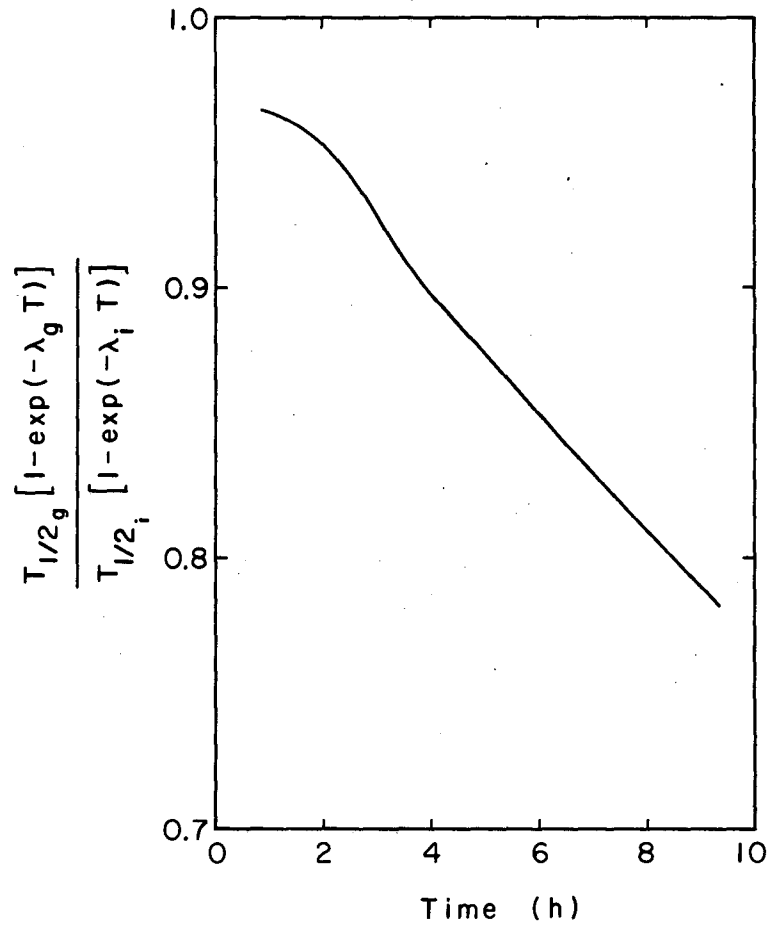
Fig. 37. The decay during bombardment correction as a function
of the time from the end of bombardment.
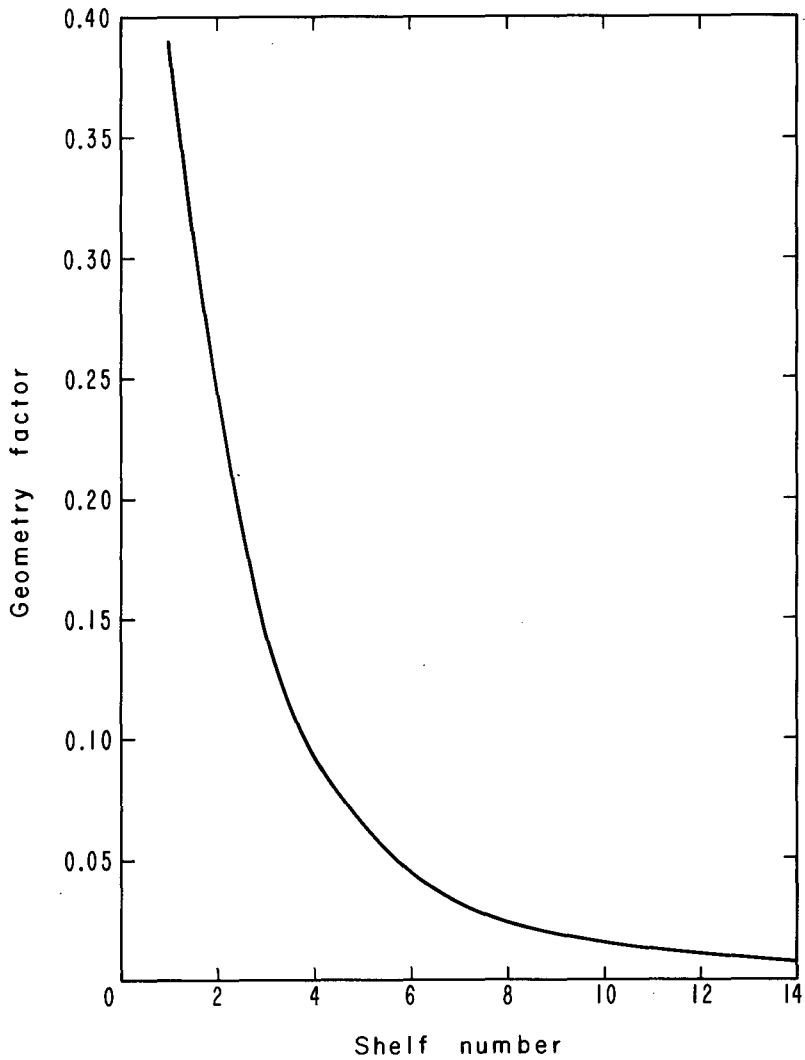
Fig. 38. The geometry of the counter as a function of the shelf
number.

LENIC also performs a least-squares analysis on a complex decay curve using expression (30). The y_i and exponential terms are premultiplied by unitary matrices so that the exponential is transformed into a form having zeros below its main diagonal. The a_j values are determined and improved until (30) is a minimum. For this program no guesses are necessary for the a_j, but accurate values of λ_j are needed and cannot be varied. The weighting factor W_i can be $1/y_i$, corresponding to data counted to equal time, or $(1/y_i)^2$ corresponding to equal statistics. The latter was used in this work. The output consists of the coefficients, the standard deviation of the coefficients, and the square of the residuals,

$$\left\{ W_i \left[y_i - \sum_{j=1}^{k} a_j \exp(-\lambda_j t_i) \right] \right\}^2 . \tag{31}$$

Both programs treat the decay curves as a sum of simple decays or

$$F = \sum_i a_i \exp(-\lambda_i t) . \tag{32}$$

For the two-component growth and decay situation of this work, Eq. (28) becomes

$$F = [\lambda_2/(\lambda_2 - \lambda_1)] A_1^0 [\exp(-\lambda_1 t) - \exp(-\lambda_2 t)] + A_2^0 \exp(-\lambda_2 t) \tag{33}$$

or

$$F = [\lambda_2/(\lambda_2 - \lambda_1)] A_1^0 \exp(-\lambda_1 t) + \{A_2^0 - [\lambda_2/(\lambda_2 - \lambda_1)] A_1^0\} \exp(-\lambda_2 t) . \tag{34}$$

Thus, in this case, the coefficients calculated by the computer are

$$a_1 = [\lambda_2/(\lambda_2 - \lambda_1)] A_1^0 \tag{35}$$

and

$$a_2 = A_2^0 - a_1 .$$

(36)

2. Parabolic Approximation

This program calculates transmission coefficients for penetration of the potential barrier by a charged particle. A parabola is used to approximate the potential function

$$V(R) = V_c + V_\ell + V_n ,$$

(37)

where

$$V_c = \frac{Z\ Z'\ e^2}{R} \quad \text{(Coulomb potential)},$$

$$V_\ell = \frac{h^2\ \ell\ (\ell + 1)}{2\ \mu\ R^2} \quad \text{(centrifugal potential)},$$

and

$$V_n = V_0 \exp\left(\frac{R_0 - R}{C}\right) \quad \text{(nuclear potential)},$$

The program finds the value of R for which $V(R)$ is a maximum for given values of the parameters V_0, R_0, and C. The transmission coefficient is then calculated by the relationship

$$T = \left\{1 + \exp\left[\frac{2\pi\ (B-E)}{\hbar\ \omega}\right]\right\}^{-1} ,$$

(38)

where

$$\hbar\ \omega = \left[\frac{\hbar\ \partial^2\ V}{\mu\ \partial r^2}\right]^{1/2} .$$

The output includes the transmission coefficient for a given ℓ value, T_ℓ , the cross section for a given ℓ value, $\sigma_\ell = \pi \textrm{\DH}^2 (2\ell + 1) T_\ell$, the total cross section, $\sigma = \Sigma \, \sigma_\ell$, and the average angular momentum, $\langle \ell \rangle = \Sigma \, \ell \, \sigma_\ell / \Sigma \, \sigma_\ell$.

The values of the parameters V_0 , R_0, and C were taken from Viola and Sikkeland, who list the best-fit values for He^4 and various heavy ions.[57] The parameter values used when He^3 was the projectile were the same as those used when He^4 was the projectile. The values for Li^7 were interpolated between those for He^4 and B^{11} .

3. Isomer-Ratio Program

The program is divided into three parts. The first part computes the partial compound-nucleus cross sections and the initial compound-nucleus spin distribution. The cross section for formation of a compound nucleus with spin J_c at a bombarding energy E is computed by using the relationship

$$\sigma (J_c , E) = \pi \textrm{\DH}^2 \sum_{s = |I-s|}^{I+s} \sum_{\ell = |J_c - S|}^{J_c + S} \frac{2 J_c + 1}{(2s+1)(2I+1)} \, T_\ell (E) ,$$

(39)

where s is the projectile spin, I is the target spin, $\textrm{\DH}$ is the de Broglie wavelength of the incoming projectile, and T_ℓ is the transmission coefficient of a projectile with orbital angular momentum ℓ and energy E. The output for this section includes J_c , $\sigma (J_c , E)$, and $P_{J_c} = \sigma (J_c , E)/\Sigma \, \sigma (J_c , E)$. The transmission coefficients used were calculated by the parabolic approximation.

The second part of the program computes the spin distribution following particle emission. The relative probability for an initial state of spin J_c for emitting a particle to a final state of spin J_f is taken as

$$\rho(J_f)_{J_c} \propto \rho(J_f) \sum_{S = |J_f-s'|}^{J_f+s'} \sum_{\ell' = |J_c-S|}^{J_c+S} T_{\ell'}(E) , \qquad (40)$$

where s' is the intrinsic spin of the emitted particle and $T'_{\ell'}(E)$ is the transmission coefficient of a particle emitted with angular momentum ℓ' and energy E. The density of states with spin J_f, $\rho(J_f)$, is proportional to $(2 J_f + 1) \exp[-(J_f + \frac{1}{2})^2/2\sigma^2]$, in which σ is the spin cutoff factor. The yield of spin J_f coming from initial spin J_c is obtained by multiplying the initial yield of $J_c (P_{J_c})$ by the fraction J_c decaying to J_f. The total yield of $J_f (P_{J_f})$ is then computed by summing over all values of J_c. This process is repeated for each value of J_f. The P_{J_f} values for the first particle emitted then become the P_{J_c} for the second emitted particle and the process continues until all particles are emitted. The transmission coefficients for the emitted neutrons ($T_{\ell'}$) were taken from Ref. 39.

The final section of the program calculates the spin distribution following γ-ray emission. The probability of decay from a state J_i to a state J_f is assumed to be proportional to the density of final states with spin J_f. The total yield of J_f is taken as

$$F_{J_f} = \sum_{J_i=|J_f-\ell|}^{J_f + \ell} \frac{F_{J_i} \rho(J_f) \delta_{J_i, J_f}}{\sum_{J_f=|J_i-\ell|}^{J_i + \ell} \rho(J_f)} \qquad (41)$$

where the level density, $\rho(J_f)$, is defined the same as above, ℓ is the multipolarity of the emitted γ ray, F_{J_i} is the initial spin distribution (following the final-particle emission or the previous γ-ray emission), and

$$\delta J_i, J_f = 1 \text{ if } |J_i - J_f| \leq \ell \leq |J_i + J_f|$$

Otherwise $\delta J_i, J_f = = 0.$

The delta function is necessary because of selection rules forbidding $0 \to 0$ transitions for $\ell = 1$ and $0 \to 1$ transitions for $\ell = 2$. The calculation using Eq. (41) is repeated for each γ ray emitted until the next-to-last emission occurs. From here, the nucleus must de-excite to either the metastable state or the ground state. This is simulated by dividing the distribution according to the spins of the two isomers. The assumption is made that the transition with the smaller spin change is the one that will occur. Thus, the states of lower spin will de-excite to the low-spin isomer while the rest feed the high-spin partner.

REFERENCES

1. Otto Hahn, Chem. Ber. 54, 1131 (1921).

2. B. V. Kurchatov, I. Kurchatov, L. Myssowski, and L. Roussinow, Compt. Rend. 200, 1201 (1935). E. Amaldi, O. D'Agostino, E. Fermi, B. Pontecorvo, and E. Segrè, Ric. Sci. 61, 581 (1935).

3. C. F. von Weizsäcker, Naturwissenschaften 24, 813 (1936).

4. Maria Goeppert Mayer and J. Hans D. Jensen, Elementary Theory of Nuclear Shell Structure (John Wiley and Sons, Inc., New York, 1955), Chap. XIII.

5. James Wing, Isomeric-Yield Ratios in Nuclear Reactions, Argonne National Laboratory Report ANL-6598, Sept. 1962 (unpublished).

6. Emilio Segrè and A. C. Helmholz, Rev. Mod. Phys. 21, 271 (1949).

7. Bernard Keisch, Phys. Rev. 129, 769 (1963).

8. Harris B. Levy, I. Isomeric States of Bismuth-210. II. Relative Yields in the Formation of Nuclear Isomers (Ph.D. Thesis), University of California Radiation Laboratory Report UCRL-2305, Aug. 1953 (unpublished).

9. J. W. Meadows, R. M. Diamond, and R. A. Sharp, Phys. Rev. 102, 190 (1956).

10. R. Serber, Phys. Rev. 72, 1114 (1947).

11. L. Katz, L. Pease, and H. Moody, Can. J. Phys. 30, 476 (1952).

12. Sylvia Mae Bailey, Independent Yields of Isomeric Pairs in Nuclear Reactions (Ph.D. Thesis), Lawrence Radiation Laboratory Report UCRL-8710, April 1959 (unpublished).

13. J. R. Huizenga and R. Vandenbosch, Phys. Rev. 120, 1305 (1960); R. Vandenbosch and J. R. Huizenga, Phys. Rev. 120, 1313 (1960).

14. James F. Mollenauer, Effects of Angular Momentum on Gamma-Ray Production in Compound Nucleus Reactions (Ph.D. Thesis), Lawrence Radiation Laboratory Report UCRL-9724, June 1960 (unpublished). J. F. Mollenauer, Phys. Rev. 127, 867 (1962).

15. J. Robb Grover, Phys. Rev. 123, 267 (1961); 127, 2142 (1962).

16. G. R. Choppin and T. J. Klingen, Phys. Rev. 130, 1990 (1963).

17. G. T. Danby, J. S. Foster, and A. L. Thompson, Can. J. Phys. 36, 1487 (1958).

18. H. Vignau and S. J. Nassiff, Nucl. Phys. 26, 108 (1961).

19. J. R. Morton, III, G. R. Choppin, and B. G. Harvey, Phys. Rev. 128, 265 (1962).

20. Thomas Darrah Thomas, Spallation-Fission Competition from the Compound System U^{233} plus He^4 (Ph.D. Thesis), University of California Radiation Laboratory Report UCRL-3791, July 1957 (unpublished).

21. C. Williamson and J. P. Boujot, Tables of Range and Rate of Energy Loss of Charged Particles of Energy 0.5 to 150 MeV, Centre d' Etudes Nucléaires de Saclay, 1962 (unpublished).

22. E. L. Hubbard, W. R. Baker, K. W. Ehlers, et al., Rev. Sci. Instr. 32, 621 (1961).

23. L. E. Glendenin, K. F. Flynn, R. F. Buchanan, and E. P. Steinberg, Anal. Chem. 27, 59 (1955).

24. G. W. Smith and F. L. Moore, Anal. Chem. 29, 448 (1957).

25. R. L. Heath, Scintillation Spectrometry Gamma-Ray Spectrum Catalogue Phillips Petroleum Company, Atomic Energy Division Report IDO-16408, 1957 (unpublished).

26. Philip A. Seeger, Nucl. Phys. 25, 1 (1961).

27. Richard Chanda (Lawrence Radiation Laboratory), private communication.

28. G. Friedlander and J. W. Kennedy, Nuclear and Radiochemistry (John Wiley and Sons, Inc., New York, 1956), Chapt. 5, p. 130.

29. W. F. Biller, Characteristics of Bismuth Fission Induced by 340 MeV Protons (Ph.D. Thesis), University of California Radiation Laboratory Report UCRL-2067, Dec. 1952 (unpublished).

30. C. F. Smith and J. D. Mahony (Lawrence Radiation Laboratory), private communication.

31. T. D. Thomas, Phys. Rev. 116, 703 (1959).

32. W. L. Hafner, Jr., J. R. Huizenga, and R. Vandenbosch, Computer Program for Calculating the Relative Yields of Isomers Produced in Nuclear Reactions, Argonne National Laboratory Report ANL-6662, Dec. 1962 (unpublished).

33. J. R. Huizenga and G. Igo, Nucl. Phys. $\underline{29}$, 462 (1962).

34. David W. Seegmiller, The Effect of Angular Momentum on the Compound Nucleus of the Ratio of the Isomers Te^{119} and Te^{119m} Produced in Low-Energy Bombardments (Ph.D. Thesis), Lawrence Radiation Laboratory Report UCRL-10850, Aug. 1963 (unpublished).

35. R. H. Fulmer, A. L. McCarthy, and B. L. Cohen, Phys. Rev. $\underline{128}$, 1302 (1962).

36. J. M. Blatt and V. F. Weisskopf, Theoretical Nuclear Physics (John Wiley and Sons, Inc., New York, 1952) Chapt. VIII.

37. D. W. Lang, Nucl. Phys. $\underline{42}$, 353 (1963).

38. J. M. B. Lang and K. J. Le Couteur, Proc. Phys. Soc. (London) $\underline{A67}$, 586 (1954).

39. A. G. W. Cameron, Can. J. Phys. $\underline{36}$, 1040 (1958).

40. G. N. Simonoff and J. M. Alexander, Angular Momentum Effects on Neutron Emission by Dy and Tb Compound Nuclei, Lawrence Radiation Laboratory Report UCRL-10099 Rev., Sept. 1962 (unpublished).

41. B. T. Feld, H. Feshbach, M. L. Goldberger, H. Goldstein, and V. F. Weisskopf, Atomic Energy Commission Report NYO-636 Jan. 1951 (unpublished).

42. V. M. Strutinski, L. V. Groshev, and M. K. Akimova, Nucl. Phys. $\underline{16}$, 657 (1960).

43. R. Vandenbosch and L. Haskin, Isomer Ratios for $Y^{87,87m}$ and the Spin Dependence of the Nuclear Level Density, Argonne National Laboratory Report (unpublished) (no date).

44. C. Block, Phys. Rev. $\underline{93}$, 1094 (1959).

45. Yu. T. Grin, Soviet Phys. JETP 16, No. 5, 1327 (1963).

46. T. Ericson and V. Strutinski, Nucl. Phys. $\underline{8}$, 284 (1958).

47. T. Ericson, Nucl. Phys. $\underline{6}$, 62 (1958).

48. D. W. Lang and K. J. LeCouteur, Nucl. Phys. $\underline{14}$, 21 (1959).

49. A. Stolovy and J. A. Harvey, Phys. Rev. $\underline{108}$, 353 (1957).

50. T. D. Newton, Can. J. Phys. $\underline{34}$, 804 (1956).

51. J. Bardeen, L. N. Cooper, and J. R. Schrieffer, Phys. Rev. $\underline{108}$, 1175 (1957).

52. Edward L. Hubbard, Range-Energy Relations for Heavy Ions in Metals, Lawrence Radiation Laboratory Report UCRL-9053, Jan. 1960 (unpublished).

53. L. C. Northcliffe and R. L. Gluckstern, The Penetration of Matter by Heavy Ions with Energies Above 1/2 MeV per AMU, Committee on Nuclear Science of the National Academy of Science National Research Council Preliminary Report, March 1961, Revised by L. C. Northcliffe, March 1962.

54. R. M. Sternheimer, Phys. Rev. 115, 137-142 (1959).

55. W. W. Mott and R. B. Sutton, in S. Flügge and E. Creutz, Eds. Handbuch der Physik, Volume XLV (Springer, Berlin, 1958).

56. D. L. Hill and J. A. Wheeler, Phys. Rev. 89, 1102 (1953).

57. V. E. Viola, Jr. and T. Sikkeland, Total Cross Sections for Fission of U^{238} Induced by He^4 and Heavy Ions, Lawrence Radiation Laboratory Report UCRL-10088, Feb. 1962 (unpublished).